Binder Jetting – Influence of shell printing on sintering densification and microstructure of 17-4 PH stainless steel

Materials & Design 268 (2026) 116465

Contents lists available at ScienceDirect

Materials & Design

journal homepage: www.elsevier.com/locate/matdes

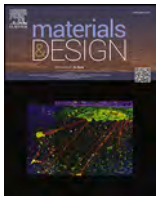

Binder Jetting – Influence of shell printing on sintering densification and microstructure of 17-4 PH stainless steel

Kai Zissel [a,b,*], Gowtham Soundarapandiyan [a], Sophie Dubiez-Le Goff [b], Eduard Hryha [a]

[a] Chalmers University of Technology, Department of Industrial and Materials Science, Rännvägen 2A, Gothenburg 41296, Sweden
[b] Linde GmbH, Carl-von-Linde-Straße 25, Unterschleißheim 85716, Germany

ARTICLE INFO

Keywords:
Binder Jetting
Shell Printing
Binder Residue
Sintering
Dilatometry
17-4 PH Stainless Steel

ABSTRACT

The shell printing strategy was utilized for Binder Jetting of 17-4 PH stainless steel to investigate the impact of the binder on green density, sintering densification, phase transformations and microstructure gradients. Green parts with 25%, 50%, 75% and 100% shell volume were printed and sintered in a dilatometer under Ar and H_2 atmospheres. The green density increased from 4.46 g/cm^3 for 25% shell volume to 4.82 g/cm^3 for 100% shell volume due to binder-induced particle rearrangement. The sintering densification in H_2 was primarily influenced by the powder packing, as higher shrinkages compensated for lower green densities, resulting in comparable sintered densities between 99.7% and 99.9%. Debinding in H_2 ensured low sintered carbon levels, resulting in high δ-ferrite fractions during sintering and martensite formation during cooling. In contrast, sintering in Ar was mainly impacted by carbon introduced by the binder since debinding efficiency was low. The increasing shell volume reduced the δ-ferrite fractions during sintering due to carbon pickup, which decreased the sintered densities from 99.3% for 25% shell volume to 93.4% for 100% shell volume. The binder-free core exhibited less porosity, higher microhardness and higher δ-ferrite fractions than the binder-affected shell, as carbon pickup stabilizes austenite during sintering and cooling.

1. Introduction

Binder Jetting (BJT) is an additive manufacturing (AM) technology, which is defined as a multi–step process according to ISO/ASTM 52900:2021 for the manufacturing of metal parts [1]. The BJT technology requires a metal powder and a liquid binder as feedstock material. The binder is utilized to provide the shape and strength of the green part but needs to be removed during the following debinding and sintering step. The binder must ensure the integrity of the green part shape until sintering neck formation begins. The debinding step should be completed until sintering densification occurs, as the binder might get trapped inside the part. In addition, the buildup of vapor pressure from debinding products might cause defects in the green part [2,3].

The difficulty of debinding depends mainly on the binder composition, the binder content, the green part's size and the powder's sensitivity to the binder composition. The polymeric binder typically contains elements such as carbon, hydrogen, oxygen, nitrogen and other trace elements, which can be introduced into the material due to incomplete debinding [4]. The change in the material's elemental composition can affect the sintering densification and sintered material properties [3,5,6]. The debinding process can be optimized by adjusting the heat treatment profile and processing atmosphere.

The difficulty of debinding can be reduced by minimizing the binder content in the green part. A promising strategy to reduce the binder content is the shell printing method, which has been explored for some materials [7–11]. Shell printing means that only the outer shell of a three–dimensional geometry is printed, enclosing the loose powder inside the shell. The shell defines the part shape and must provide sufficient green strength. Consequently, the green part can be separated into the binder-affected shell and binder-free core regions with the unbound and loosely packed powder.

Shell printing offers several advantages for BJT. The printing process can save time as less binder volume is deposited [7]. Moreover, the binder consumption per part can be reduced [8], saving costs and reducing carbon dioxide (CO_2) emissions, increasing the sustainability of the BJT process. The most significant advantage is the reduced risk of binder contamination as the difficulty of debinding decreases. Additionally, the time of the debinding process can be minimized [8], which can potentially remove the need for conventional debinding dwell steps. This can be especially beneficial for large components, where debinding

* Corresponding author at: Chalmers University of Technology, Department of Industrial and Materials Science, Rännvägen 2A, Gothenburg 41296, Sweden.
E-mail address: zissel@chalmers.se (K. Zissel).

https://doi.org/10.1016/j.matdes.2026.116465
Received 21 March 2026; Received in revised form 28 May 2026; Accepted 18 June 2026
Available online 22 June 2026

might require long holding times. Furthermore, the requirements on the debinding atmosphere can potentially be reduced, as efficient binder decomposition might require oxidizing or reducing species in the atmosphere.

The shell printing, however, is limited to a minimum shell thickness that needs to provide sufficient strength to the green part. As the shell thickness decreases, the depowdering and handling of green parts become more challenging as the risk of breaking increases. In addition, overhanging features are more prone to distortion and cracking as less binder provides stability during the debinding process until sintering neck formation begins [9]. Furthermore, uncertainty arises as the uneven distribution of the binder might impose property gradients in the green and sintered parts. In addition, the shell and wall thickness ratio might vary across the part, influencing the sintering shrinkage anisotropy [9].

Research on shell printing demonstrated that the binder affects powder packing during printing. Miao et al. [10] reported for shell printing of alumina powder that the green density increased slightly with the shell volume fraction for powders with a D_{50} of 10 μm and 23 μm, respectively. In contrast, a decline in green density with increasing shell volume was found for a D_{50} of 77 μm [10]. The authors argued that the powder-binder interaction could potentially rearrange powder particles and increase the powder packing due to the capillary bridging [10]. The ratio of the particle size distribution (PSD) and layer thickness influenced whether the shell or core had a higher powder packing [10].

Rahman et al. [9] reported that the green density decreased when the shell thickness was increased for BJT printing of copper powder. Khademitab et al. [8] found that the relative green density for 316L stainless steel powder was 50% for a bulk sample, while it increased to 54% for a shelled geometry with 0.5 mm thickness. A crack between the shell and the core of the sample in the green state was identified by micro-computed tomography [8]. The interface between the core and shell can become a crack initiation area due to increased porosity [8,9].

Studies on the binder deposition during printing demonstrated that the binder can also cause powder ejection upon impact of the binder droplet onto the powder bed, resulting in areas of increased porosity [12,13]. Parab et al. [12] observed the ballistic effect of the binder via high–speed X-ray imaging, which both shifted the particles under the droplet and ejected particles from the powder bed. Lawrence et al. [13] conducted a thorough investigation on the interaction between binder droplet and powder by high-speed synchrotron X-ray imaging, demonstrating that the powder ejection is influenced by several parameters such as powder characteristics, spreading conditions and pre-wetting of the powder bed.

Several studies on shell printing reported the detrimental impact of the binder on sintering densification. Rahman et al. [9] registered for shell printing of copper that the highest sintered density of 93.30% was achieved for 0.5 mm shell thickness, while the lowest of 88.72% was obtained for the bulk sample. The low densification was explained by binder residue from binder pyrolysis trapped inside the interparticle spaces, which impairs inter-particle neck formation for sintering [9].

Frykholm et al. [7] identified that the shell printing strategy could improve the sintered densities of 316L stainless steel, as the binder had a detrimental impact on sintering densification. Mariani et al. [11] found for shell printing of 316L stainless steel that the porosity concentrated in the shell region, while the core was nearly fully dense [11]. This was attributed to the binder–generated microporosity and carburization, which reduces the densification rate [11].

The previous research on shell printing suggests that the effect of the binder on powder packing and sintering densification might vary depending on the material and powder characteristics, binder formulation, printer hardware and process parameters. While previous studies have demonstrated the potential of shell printing to reduce binder consumption, a systematic understanding of how spatial variations in binder content influence powder packing, sintering densification, microstructural evolution and material properties locally remains lacking.

Furthermore, it remains unclear whether reducing the binder content through shell printing can eliminate the need for conventional debinding dwell steps and thereby reduce processing time. Another unresolved question is whether a reduced binder content can also lower the requirements on the processing atmosphere, enabling sufficient debinding under an inert argon (Ar) atmosphere compared to a reactive hydrogen (H_2) atmosphere.

In addition, the shell printing has not yet been studied for 17-4 PH stainless steel, which is sensitive to carbon and oxygen content and is a popular choice for binder-assisted processing technologies [6,14]. Zissel et al. [15] demonstrated for BJT of 17-4 PH stainless steel that a high binder residue can harm the sintering densification due to carbon pickup in the material. Therefore, 17-4 PH represents a particularly relevant material for examining the influence of binder content by shell printing.

Consequently, this study systematically investigates the influence of binder content and its distribution on powder packing, sintering densification, phase transformations and microstructure gradients for shell printing of 17-4 PH stainless steel. Shelled cuboid samples with 25%, 50%, 75% and 100% shell volume were printed and sintered in a dilatometer to evaluate the shrinkage over temperature and time. The sintering was performed without a debinding dwell step in reactive H_2 gas and compared to processing under inert Ar to assess whether the shell printing strategy can reduce the requirements on the processing atmosphere. The obtained sintered densities, shrinkages, microstructure and material chemistry were correlated. Gradients in the porosity, pore diameters, microstructure and microhardness were analyzed in detail.

2. Materials and methods

2.1. Materials and printing

The raw materials used in this study were 17-4 PH stainless steel powder (17-4 PH, Desktop Metal, USA) and a water-based binder (SPJ-04, Desktop Metal, USA) with a density of 1.04 g/cm^3. The powder's particle size distribution was determined to be $D_{10} = 7$ μm, $D_{50} = 16$ μm and $D_{90} = 30$ μm. The powder density was 7.82 g/cm^3, measured by a helium pycnometer (AccuPyc 1330, Micromeritics Instrument Corp., USA). Printing was performed on a Production System™ P-1 (Desktop Metal, USA) in a nitrogen atmosphere with a controlled relative humidity of 40%. The as-received powder oxygen content was 1163 ± 8 ppm. The carbon content was 205 ppm. The chemical composition of the powder complies with the MPIF35/ASTM B883 - 24 standards for Metal Injection Molding (MIM) [16,17].

The shell printing strategy was utilized to investigate the effect of the binder on green density and sintering densification. The shell printing approach followed in this study is visualized in Fig. 1. Cuboid samples with consistent dimensions of 10 x 10 x 10 mm^3 were printed with four different shell thicknesses. The shell thicknesses were 0.46 mm, 1.03 mm, 1.85 mm and 5.00 mm, corresponding to shell volume fractions of 25%, 50%, 75% and 100%. The 100% shell volume corresponded to the standard printing of a bulk sample. The shell thickness and volume percentages refer to the nominal geometry. The binder was only deposited in the shell areas, as depicted by the two-dimensional binder printing patterns.

Table 1 lists the main printing and binder saturation parameters used in this study. Note that the binder printing pattern varied slightly, as the slicing software defines different printing patterns based on the feature region and size, such as an inner saturation. All parameters were kept constant for all samples. The slicing software calculates the amount of binder needed for printing, which is listed in Fig. 1 for each shell thickness.

The carriage velocity refers to the movement speed of the build box, which is moving in X-direction during printing, while the powder dispensing unit, powder compaction roller and printhead are stationary modules. The adjustable parameters powder metering ratio and powder

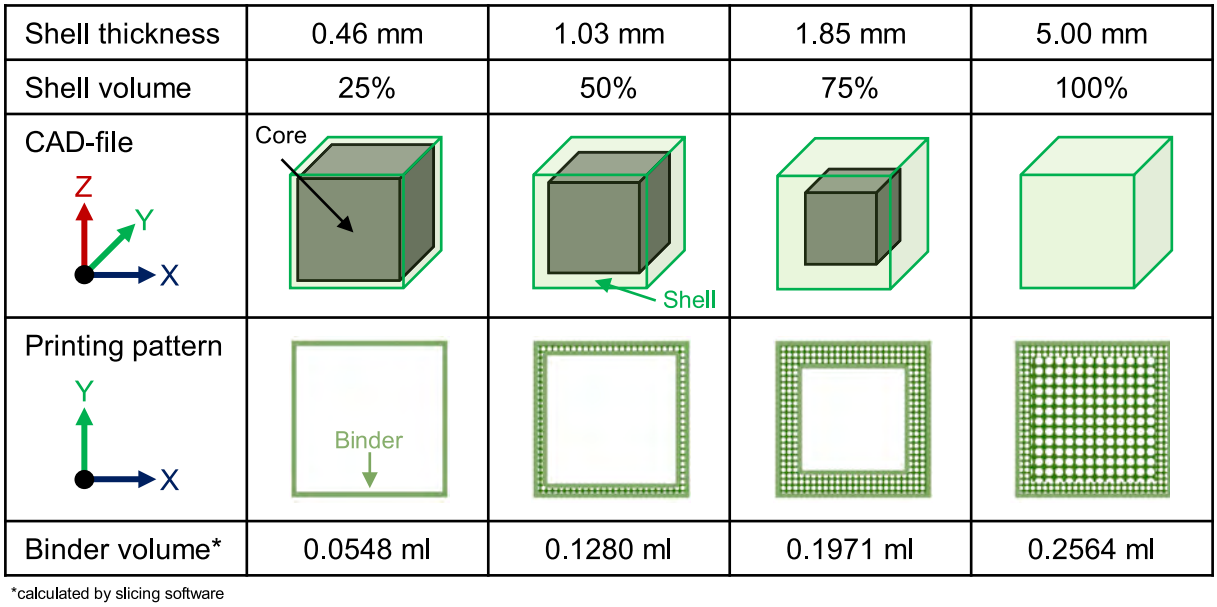

Fig. 1. Shell printing strategy followed in this study with 25%, 50%, 75% and 100% shell volume.

Table 1
Main printing and binder saturation parameters.

Layer thickness	Carriage velocity (build box)	Powder metering ratio	Powder compaction ratio	Relative humidity	Oxygen level	Shell saturation	Inner shell saturation	Inner saturation
65 μm	550 mm/s	2.2°/mm	4°/mm	40%	<2.2%	66%	50%	45%

compaction ratio are defined as the number of degrees that the rollers are rotated in 1 mm of linear travel of the carriage (build box). This corresponds to a compaction roller rotation of 2200°/s for a carriage velocity of 550 mm/s.

The layout of the build job is demonstrated in Fig. 2, which displays the binder printing pattern of layer 88, which is close to the middle of the build job. The X-direction was the powder spreading direction, the Y-direction was parallel to the axis of the compaction roller and the Z-direction was the build direction. Note that the first and last couple of layers differ from layer 88, as the binder is fully deposited onto the cross-section at the bottom and top of the cuboid samples in order to form a three-dimensional shell enclosing the loose powder.

After printing, the build box was placed in a furnace (TR 120 LS, Nabertherm GmbH, Germany) for curing at 200°C for 4 h to remove water and solvents and to trigger the crosslinking of the binder. A vial was filled with 0.5 g of liquid binder and put under the curing process at 200°C for 4 h to approximate the percentage of remaining binder mass after curing.

Furthermore, the cured binder mass in the green sample was approximated by measuring the mass loss after debinding at 300°C for 2 h in air for one sample per shell volume. This debinding cycle is based on a previous study using the same 17-4 PH powder and binder composition, which led to nearly complete binder removal [4].

The green part's mass and dimensions were measured after

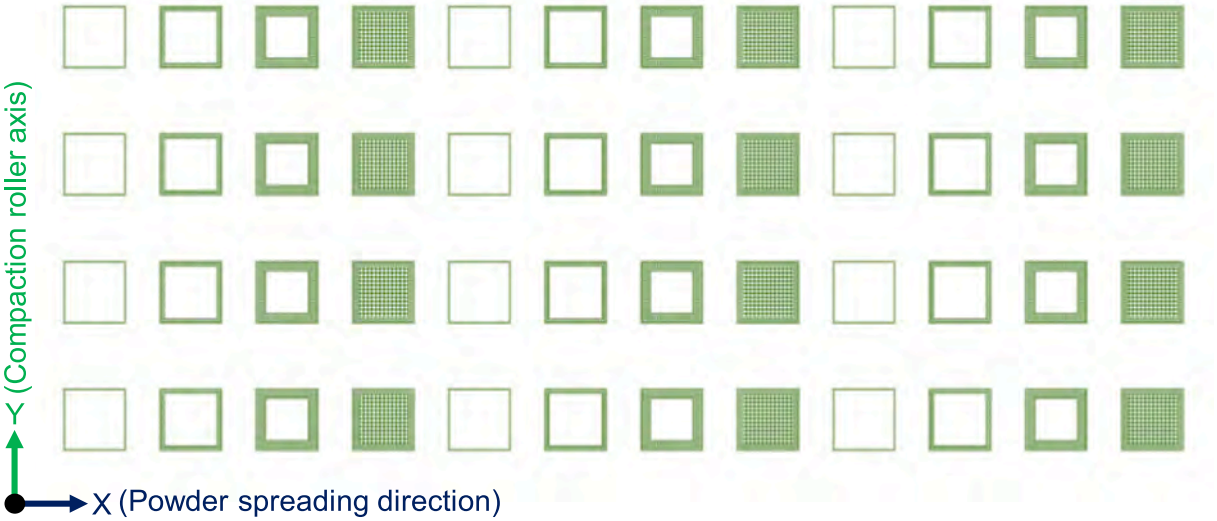

Fig. 2. Binder printing pattern of layer 88 used for varying shell thicknesses of cuboid samples.

depowdering utilizing a precision scale with a resolution of 0.001 g and a micrometer screw gauge with a resolution of 1 μm. The dimensions were used to calculate each sample's volume and green density. For each shell volume, 12 samples were obtained from the build job and measured.

2.2. Dilatometry

To assess the impact of the shell printing and binder on the sintering densification, the samples were sintered in a dilatometer with a horizontal pushrod (L75HS1600C, Linseis Messgeräte GmbH, Germany), measuring the shrinkage over time and temperature. All samples were measured in the powder spreading direction (X-direction). The printing orientation, dilatometry setup and metallographic cutting procedure are sketched in Fig. 3.

The pushrod force was set to 300 mN and the measuring frequency was 60 Hz. The sintering cycle consisted of heating up to 1300°C at 5°C/min and holding for 60 min at 1300°C. The cooling rate after sintering was controlled at 5°C/min. For each shell volume, two processing gases were compared. Hydrogen (H_2) was chosen as a common atmosphere for sintering of 17-4 PH due to its reducing capabilities. The other process gas was argon (Ar), which does not influence binder and powder reactions due to its inert nature. The gas flow through the capillary was set to 300 ml/min and the purge gas flow to 100 ml/min.

No additional debinding dwell time was added to the described thermal cycle to explore the potential of minimizing thermal processing times by shell printing. One sample was measured for each combination of shell volume and processing atmosphere. The sintered dimensions were measured in X-, Y- and Z-direction after dilatometry with a micrometer screw gauge for each sample individually to examine potential sintering shrinkage anisotropy.

2.3. Analysis of sintered specimens

After sintering, the sample's dimensions and mass were determined as described for the green parts. This allowed the shrinkages in X-, Y- and Z-direction, as well as the sintered density, to be determined. The density was additionally measured by Archimedes' principle. The samples were cut in the XY-plane for metallographic analysis.

One half was hot embedded, ground and polished to analyze the porosity and microstructure by light optical microscopy (LOM) (VHX 6000, Keyence, Germany). Stitched images of the whole cross-section were taken at a magnification of 300x with a resolution of 1.6 pixels/μm. The image analysis software ImageJ was used to determine the porosity of the LOM images. Each cross-section was re-grinded two times in order to obtain three stitched LOM images per sample to determine the overall porosity.

Additionally, the distribution of the porosity and pore diameters was analyzed for one representative cross-section per sample by dividing the stitched image into sections. An ROI of 8100 x 8100 μm was defined and divided into a 10 x 10 grid, corresponding to 810 x 810 μm per section. Each section was analyzed to create a contour plot of the porosity and pore diameter distribution. The equivalent pore diameter was calculated based on the pore area, assuming an ideal circle. The Vickers microhardness and its distribution along the sample cut were measured using a hardness tester (DuraScan 10, EMCO-TEST Prüfmaschinen GmbH, Germany) with a load of 0.98 N (HV0.1). Indents were taken in pore-free areas with spacings of 0.8 mm to form an 11 x 11 grid.

Electron backscatter diffraction (EBSD) analysis was performed using a field emission gun scanning electron microscope (Gemini 450 FEG-SEM, Carl Zeiss AG, Germany) equipped with an Oxford Symmetry EBSD detector. The measurements were performed at an accelerating voltage of 20 kV and a probe current of 10 nA to investigate bcc and fcc phase fractions along with the grain orientation. A magnification of 350X and a step size of 0.4 μm was used for all samples. The acquired maps were post-processed in AZtecCrystal software (Oxford Instruments, UK) for removal of wild spikes and zero-solution points using an eight-nearest-neighbor clean-up routine. Three mappings were conducted from the fringe to the core of samples with 25% and 100% shell volume sintered in Ar or H_2. The δ-ferrite fractions of the microstructure were quantified with the Trainable Weka Segmentation plugin of the image analysis software Fiji (open-source).

The other halves of each sample cut were used to measure the carbon, oxygen, nitrogen and hydrogen contents. The carbon content was obtained from a C/S analyzer (CS 2000, ELTRA GmbH, Germany), while the other three elements were determined by an ONH analyzer (ONH836, LECO Corporation, USA).

Thermodynamic simulations (JMatPro 14.0, Sente Software Ltd., United Kingdom) were utilized to predict the impact of carbon on phase fractions and phase transformations during the cooling of 17-4 PH stainless steel. The alloy composition was set to Fe-17.54Cr-4.21Ni-4.2Cu-0.68Mn-0.07Mo-0.29Nb-0.74Si. Carbon contents of 0.02 wt%, 0.10 wt% and 0.20 wt% were compared. The cooling rate was set to 5°C/min and a grain size of 25 μm was assumed.

3. Results

3.1. Impact of binder content and shell printing on green density

The liquid binder volume provided by the slicing software was used to calculate the liquid binder mass deposited into the green part during printing based on the liquid binder density of 1.04 g/cm^3. After curing at 200°C for 4 h, the liquid binder mass in a vial decreased by 82 wt%. It was assumed that a similar mass reduction occurred within the green parts after curing.

Fig. 4 shows the calculated binder mass remaining in the green part after curing for 25%, 50%, 75% and 100% shell volume. The binder mass increased nearly linearly with the shell volume. In addition, the debinding mass losses, measured after debinding at 300°C for 2 h in air, were plotted in Fig. 4. The debinding mass losses were slightly lower than the corresponding calculated binder mass, indicating slight binder residue. 17-4 PH green parts printed with the same binder demonstrated

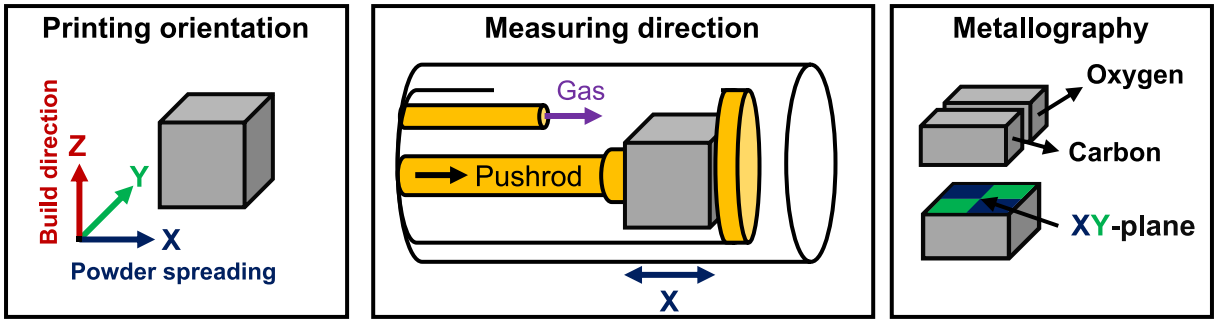

Fig. 3. Orientation of the samples during printing, dilatometry and metallography.

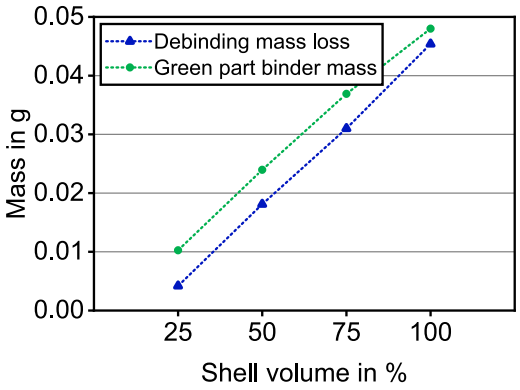

Fig. 4. Calculated binder mass remaining in a green part after curing and measured debinding mass losses (300°C for 2 h in ambient air) for samples with 25%, 50%, 75% and 100% shell volume. (For interpretation of the references to colour in this figure legend, the reader is referred to the web version of this article.)

in a previous study that debinding in air at 300°C for 2 h removed most of the binder [4]. Note that the debinding experiment at 300°C for 2 h in air was only utilized to estimate the binder mass in the green part and is not applied in the sintering trials.

Fig. 5 demonstrates the influence of the shell volume on the mass, volume, density and printing accuracy of the green part. The dimensional deviations refer to the nominal dimensions of the samples. In addition, the calculated binder mass was subtracted to assess its significance on the overall green part mass and density. The green part mass increased considerably by ~0.29 g from 25% to 100% shell volume, while the binder mass increased only by ~0.04 g.

The green part volume for 25% shell volume was close to 1 cm^3, but decreased to 0.985 cm^3 for 100% shell volume. The decrease in the volume can be seen in the dimensional deviations relative to the nominal dimensions of 10 mm. With increasing shell volume, the dimensional deviations shifted to more negative values, mainly for the Y- and Z-direction. The largest dimensional deviations were observed in the X-direction, which may be attributed to the movement of the build box along this axis, potentially making dimensional control more challenging.

The green densities increased nearly linearly from 4.46 ± 0.01 g/cm^3 for 25% shell volume to 4.82 ± 0.04 g/cm^3 for 100% shell volume, corresponding to an increase of 0.36 g/cm^3 or ~8%. The contribution from added binder to the green component density increased from ~0.01 g/cm^3 to ~0.05 g/cm^3, corresponding to an increase of ~0.04 g/cm^3. Hence, the binder comprised only ~11% of the density increase. The binder weight fraction increased from 0.22 wt% for 25% shell volume to 1.01 wt% for 100% shell volume.

3.2. *Influence of binder content and green density on sintering densification*

3.2.1. *Dilatometry*

Fig. 6 displays the dimensional change in X-direction during sintering in Ar for the cuboid samples with 25%, 50%, 75% and 100% shell volume. Note that shrinkage refers to negative values of dimensional change. The highest shrinkage of 15.15% was found for 25% shell volume, which decreased significantly by 2.34% for 50% shell volume. The shrinkage was further reduced by 1.56% from 50% to 75% shell volume. The shrinkage for 100% shell volume exhibited only a marginal decrease of 0.40% compared to 75% shell volume. During cooling, a phase

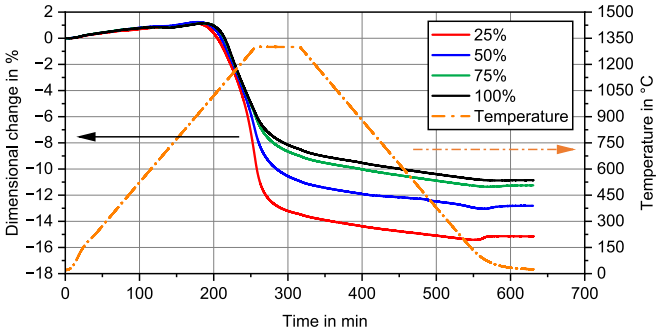

Fig. 6. Dilatometric curves in X-direction for 25%, 50%, 75% and 100% shell volume sintered in Ar.

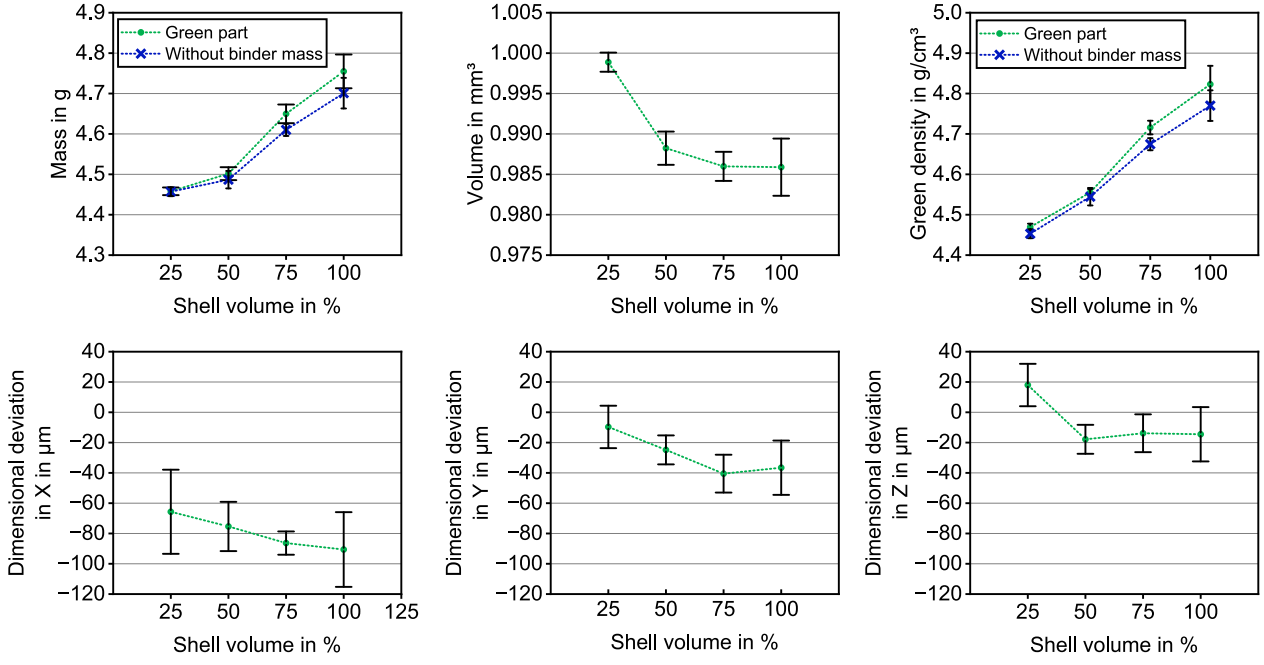

Fig. 5. Mass, volume, density and dimensional deviations of green parts printed with 25%, 50%, 75% and 100% shell volume. (For interpretation of the references to colour in this figure legend, the reader is referred to the web version of this article.)

transformation, signaled by a linear dimensional increase of the samples, was registered for 25% and 50% wall volume, which was not notable for 75% and 100% shell volume.

The dimensional change rate for processing in Ar is shown in Fig. 7 for the varying shell volumes. The start of sintering shrinkage was noted at ~891°C for 25% shell volume, ~908°C for 50% shell volume and ~951°C for both 75% and 100% shell volume.

The highest shrinkage rate for 100% shell volume was registered at ~1146°C, while a second peak was observed at ~1290°C. For 75% shell volume, the dimensional change rate followed a trend comparable to 100% shell volume until ~1110°C. A second peak in the shrinkage rate began to appear at ~1253°C for 75% shell volume. For 50% shell volume, a notable increase in the shrinkage rate appeared at ~1126°C. The highest peak shrinkage rate was observed for 25% shell volume, where a rapid increase was noticed from ~1133°C. A rapid expansion during cooling after sintering was observed for 25% shell volume starting at ~119°C. A similar expansion was registered starting at a lower temperature of ~79°C for 50% shell volume. For 75% and 100% shell volume, a slight expansion was indicated at similar temperatures during cooling.

The dilatometric curves of the sample sintered in H_2 for 25%, 50%, 75% and 100% shell volume are displayed in Fig. 8. The final shrinkage decreased by 0.60% from 25% to 50% shell volume, by 0.70% from 50% to 75% shell volume and by 0.53% from 75% to 100% shell volume. All samples showed a notable linear expansion during the cooling stage.

Fig. 9 displays the dimensional change rate for sintering in H_2 for the varying shell volumes. The onset of sintering shifted slightly to higher temperatures from 854°C to 895°C with increasing shell volume from 25% to 100%. The dimensional change rate showed similar behavior for all samples until 1077°C, after which differences emerged. A rapid increase in the shrinkage rate was observed, with the sintering shrinkage peak shifting to slightly lower values and higher temperatures with increasing shell volume. The sudden rise of the shrinkage rate began at 1162°C for 25% shell volume, at 1183°C for 50% shell volume, at 1192°C for 75% shell volume and at 1198°C for 100% shell volume. During cooling, a rapid expansion was measured starting at ~166°C for 25% and 50% shell volume. For 75% and 100%, the start of the expansion decreased slightly to lower temperatures of 160°C and 162°C, respectively.

The final shrinkages and maximum shrinkage rate are summarized in Table 2 for the different shell volumes sintered in Ar and H_2. Samples sintered in H_2 showed considerably higher shrinkages for 50%, 75% and 100% shell volume than Ar. For 25% shell volume, the shrinkage was only 1% higher in H_2 than in Ar. The maximum shrinkage rate shifted to higher temperatures with increasing shell volume for sintering in H_2.

3.2.2. *Sintered density, shrinkage anisotropy and microstructure*

Fig. 10 depicts the densities of samples sintered in Ar and H_2 for the varying shell volumes. The sintered densities decreased for sintering in Ar when the shell volume increased. The highest density of 7.30 ± 0.03 g/cm^3 was obtained for 25% shell volume, while the lowest density was 6.70 ± 0.03 g/cm^3 for 100% shell volume. The results from LOM confirmed the trend with 99.3 ± 0.2% density for 25% shell volume and 93.4 ± 1.8% density for 100% shell volume.

Sintering in H_2 showed minor differences in the final sintered densities. The highest density of 7.58 ± 0.01 g/cm^3 was measured for 50% shell volume, closely followed by 7.56 ± 0.01 g/cm^3 for 25% shell volume. 75% and 100% shell volume resulted in similar densities of 7.52 ± 0.02 g/cm^3. The porosity analysis of the cross-sections also indicated the trend. The mean LOM-based densities of the samples processed in H_2 ranged from 99.7 ± 0.1% to 99.9 ± 0.0%.

The densities determined by Archimedes' principle were generally higher than the geometry–based densities. This could be linked to the surface roughness, affecting the measurement with a micrometer screw gauge or caliper [18]. In addition, geometry-based density determination assumes an ideal cuboid. Both methods do not allow to take into consideration the impact of phase composition (fraction of δ-ferrite and retained austenite) on the final density.

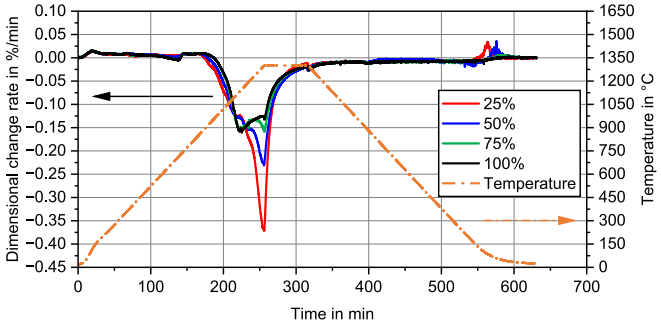

Fig. 7. Dimensional change rate in X-direction for 25%, 50%, 75% and 100% shell volume sintered in Ar.

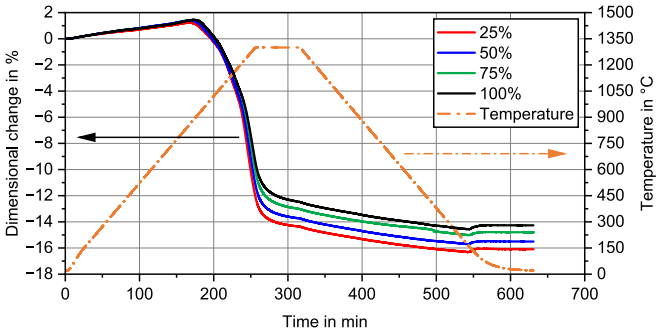

Fig. 8. Dilatometric curves in X-direction for 25%, 50%, 75% and 100% shell volume sintered in H_2.

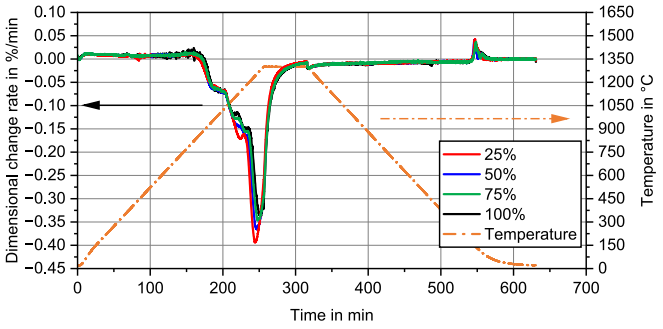

Fig. 9. Dimensional change rate in X-direction for 25%, 50%, 75% and 100% shell volume sintered in H_2.

Table 2
Summary of final shrinkage and maximum shrinkage rate obtained from dilatometry trials.

Shell volume in %	Processing atmosphere	Final shrinkage in %	Temperature of maximum shrinkage rate in °C	Maximum shrinkage rate in %/min
25	Ar	−15.15	1299	−0.37
50	Ar	−12.81	1299	−0.23
75	Ar	−11.25	1300	−0.16
100	Ar	−10.85	1146	−0.13
25	H_2	−16.10	1243	−0.39
50	H_2	−15.50	1258	−0.36
75	H_2	−14.80	1263	−0.35
100	H_2	−14.27	1280	−0.33

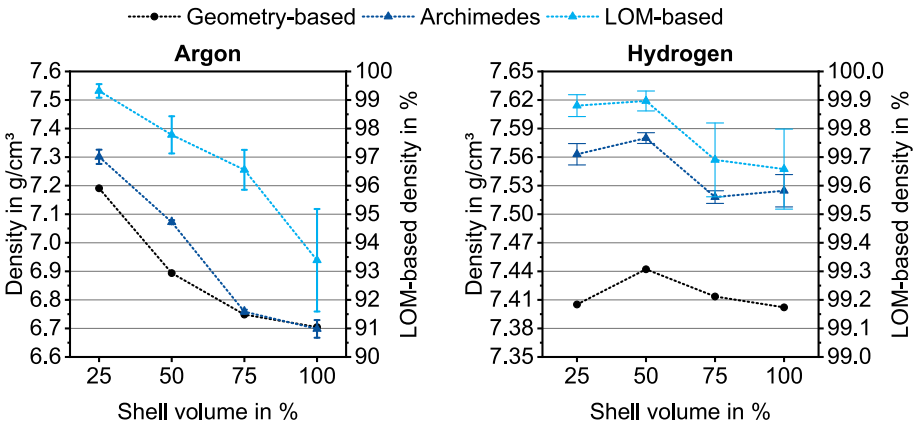

Fig. 10. Sintered densities determined via geometry, Archimedes' principle and light optical microscopy (LOM) for varying shell volumes sintered in Ar and H_2.

Table 3 lists the density increase calculated by the green and sintered densities (geometry-based density). The calculations demonstrate that the densification decreased in both atmospheres from 25% to 100% shell volume. Sintering in H_2 resulted in higher densification than Ar, where the lowest difference between the two atmospheres was found for 25% shell volume and the most significant difference for 75% shell volume.

The sintering shrinkages in the X-, Y- and Z-direction are presented in Fig. 11, which were calculated by the measured green and sintered dimensions for each sample individually. The trend of reduced shrinkage for increased shell volume was confirmed for all three directions. An anisotropy in the shrinkage was evident for all samples under both processing atmospheres. The Z-direction (build direction) showed notably higher shrinkages than the X- and Y-direction for both processing gases. This phenomenon is common for BJT and is caused by areas of increased porosity in the build direction between two deposited powder layers, leading to higher shrinkage [18,19]. A detailed analysis of the sintering anisotropy by high-resolution synchrotron X-ray computed tomography (SXCT) is given elsewhere [20]. For sintering in Ar, the shrinkage in the X- and Y-direction was similar, but the samples showed slightly higher values in the X-direction under H_2 atmosphere.

Fig. 12 compares the microstructure for the core and fringe of the samples sintered in Ar. For 25% shell volume, δ-ferrite was observed along grain boundaries, commonly formed during the sintering of 17-4 PH stainless steel [6,14]. The fraction of δ-ferrite seemed comparable for the core and fringe of the sample. For 50% shell volume, δ-ferrite was observed at the core of the specimen, but only a small fraction of δ-ferrite was found at the edge of the sample. For 75% shell volume, the δ-ferrite fraction in the core decreased considerably compared to 25% and 50% shell volume and no δ-ferrite was registered towards the edge. No δ-ferrite was present at the core and fringe of the cross-section for 100% shell volume sintered in Ar.

Fig. 13 shows the microstructure at the core and fringe of the samples sintered in H_2 for 25%, 50%, 75% and 100% shell volume. In contrast to sintering in Ar, the δ-ferrite phase was registered for the core and fringe of all samples. The fraction of δ-ferrite was significantly higher after sintering in H_2 than the fractions observed for sintering in Ar.

3.2.3. *Sintered chemistry and thermodynamic considerations*

Fig. 14 presents the carbon and oxygen content of the samples for 25%, 50%, 75% and 100% shell volume after sintering in Ar and H_2. The oxygen content for samples sintered in Ar decreased with increasing shell volume from 745 ppm to 63 ppm, while it increased slightly from 65 ppm to 141 ppm for sintering in H_2. The carbon content increased between 25% and 75% shell volume from 289 ppm to 1242 ppm, while it reduced to 994 ppm for 100% shell volume. The carbon contents for sintering in H_2 were below 200 ppm for all shell volumes. The nitrogen contents dropped below 80 ppm and the hydrogen contents dropped below 5 ppm for all sintered samples.

Table 3
Density increase for varying shell volumes after sintering in Ar and H_2.

Shell volume in %	25	50	75	100
Density increase for Ar in %	61.2	51.6	42.6	40.4
Density increase for H_2 in %	66.4	61.5	57.5	51.9

The phase composition of 17-4 PH depends upon the elemental composition of the material, which is sensitive to the carbon content [5,15]. The evolution of the phase fractions of austenite, ferrite and martensite during cooling from 1300°C with 5°C/min are highlighted in Fig. 15 for sintered carbon contents of 0.02 wt% (200 ppm), 0.10 wt% (1000 ppm) and 0.20 wt% (2000 ppm).

For 0.02 wt% carbon, a phase fraction of 49 vol% for δ-ferrite was predicted at 1300°C. The δ-ferrite transforms into austenite upon cooling and ultimately into martensite at 120°C with a phase fraction of 76 vol%, accompanied by a rapid decrease in the density. For 0.10 wt% carbon, the fraction of δ-ferrite at 1300°C decreased notably to 24 vol%. The martensite formation shifted to 75°C with a final martensite fraction of 54 vol%. For 0.20 wt% carbon, the δ-ferrite at 1300°C reduced to 3 vol % and no martensite formation occurred.

3.3. *Influence of shell printing on gradients in porosity, pore diameter and hardness*

Fig. 16 visualizes the distribution of the porosity, equivalent pore diameters and microhardness across the XY-plane for 25%, 50%, 75% and 100% shell volume sintered in Ar. The dimensions in Fig. 16 correspond to the sintered dimensions after sintering shrinkage. The dashed lines portray the interface between the core and the shell. For 25% shell volume, the core exhibited a porosity of ~0.4%, while the porosity reduced slightly toward the edge. The pore diameters were, however, lower in the core than in the shell of the sample with 25% shell volume. The microhardness distribution was mostly homogenous, with a mean value of 307 ± 27 HV0.1 for 25% shell volume.

For 50% shell volume, the porosity in the core was low at ~1.4%, while it increased to ~2.6% in the shell. The core exhibited slightly smaller pore diameters of ~3.5 μm compared to the shell of ~4.1 μm. The microhardness increased considerably from ~250 HV0.1 in the shell to ~325 HV0.1 in the core.

For 75% shell volume, the core exhibited notably lower porosity in the core compared to the shell. The pore diameters slightly decreased towards the top right corner of the core region, while the shell showed comparable pore sizes. An apparent microhardness gradient occurred from the fringe with values below 200 HV0.1 to the core of the sample with values above 300 HV0.1.

For 100% shell volume, a considerable gradient in porosity was found in the X-direction for 100% shell volume, where the porosity

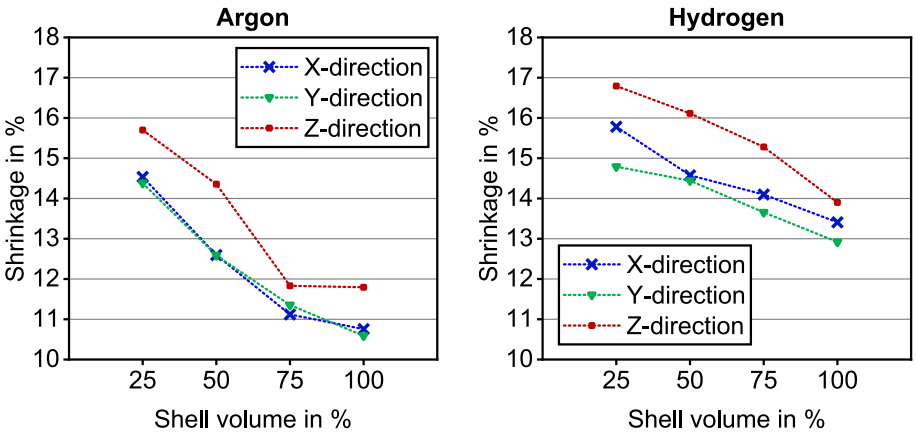

Fig. 11. Shrinkage in X-, Y- and Z-direction for different shell volumes sintered in Ar and H_2.

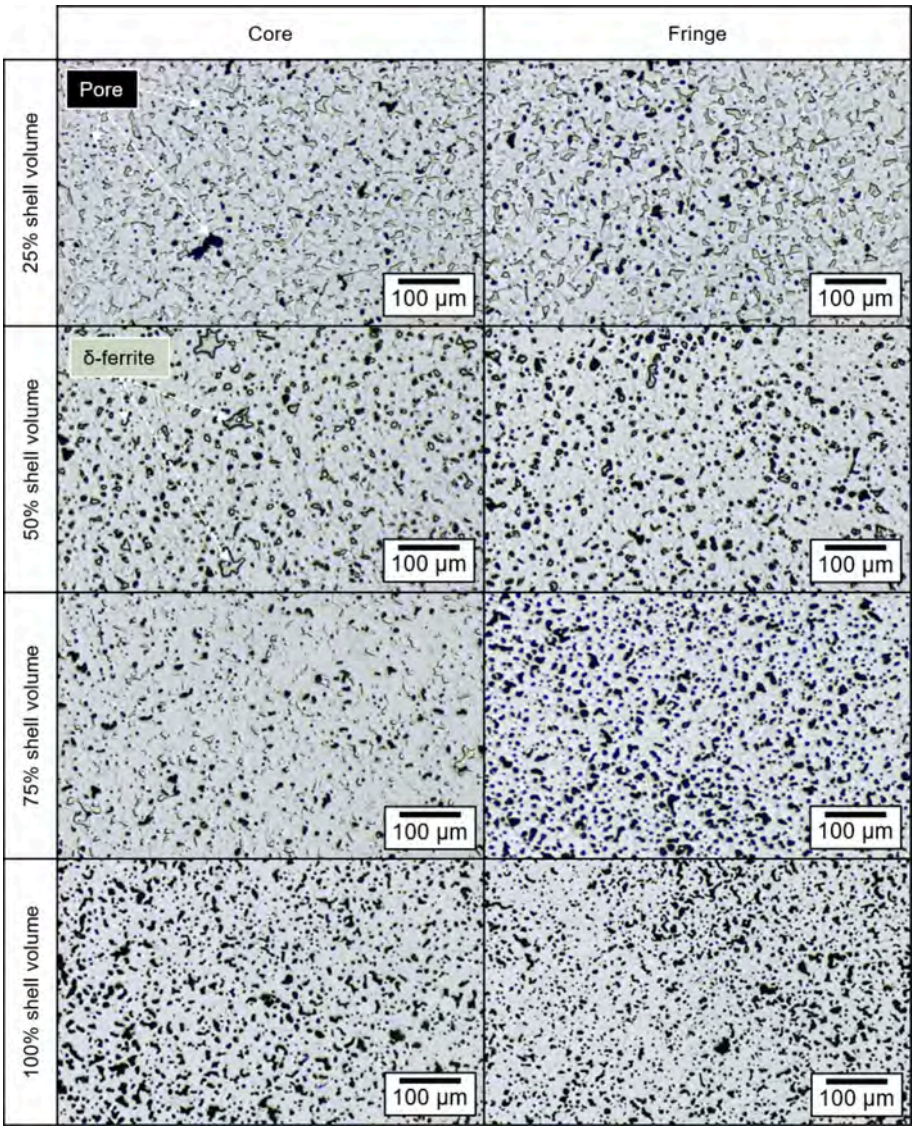

Fig. 12. Microstructure at the core and fringe of the samples sintered in Ar for 25%, 50%, 75% and 100% shell volume.

increased to values of over 10% towards positive coordinates in the X-direction. Nevertheless, the pore diameters were comparable for the whole cross-section. The microhardness was similar for the entire cross-section, with a mean of 176 ± 21 HV0.1, which was significantly lower compared to 25% shell volume.

Fig. 17 highlights the distribution of porosity, equivalent pore diameters and microhardness for the samples with 25%, 50%, 75% and 100% shell volume sintered in H_2. Note that the color scale differs from

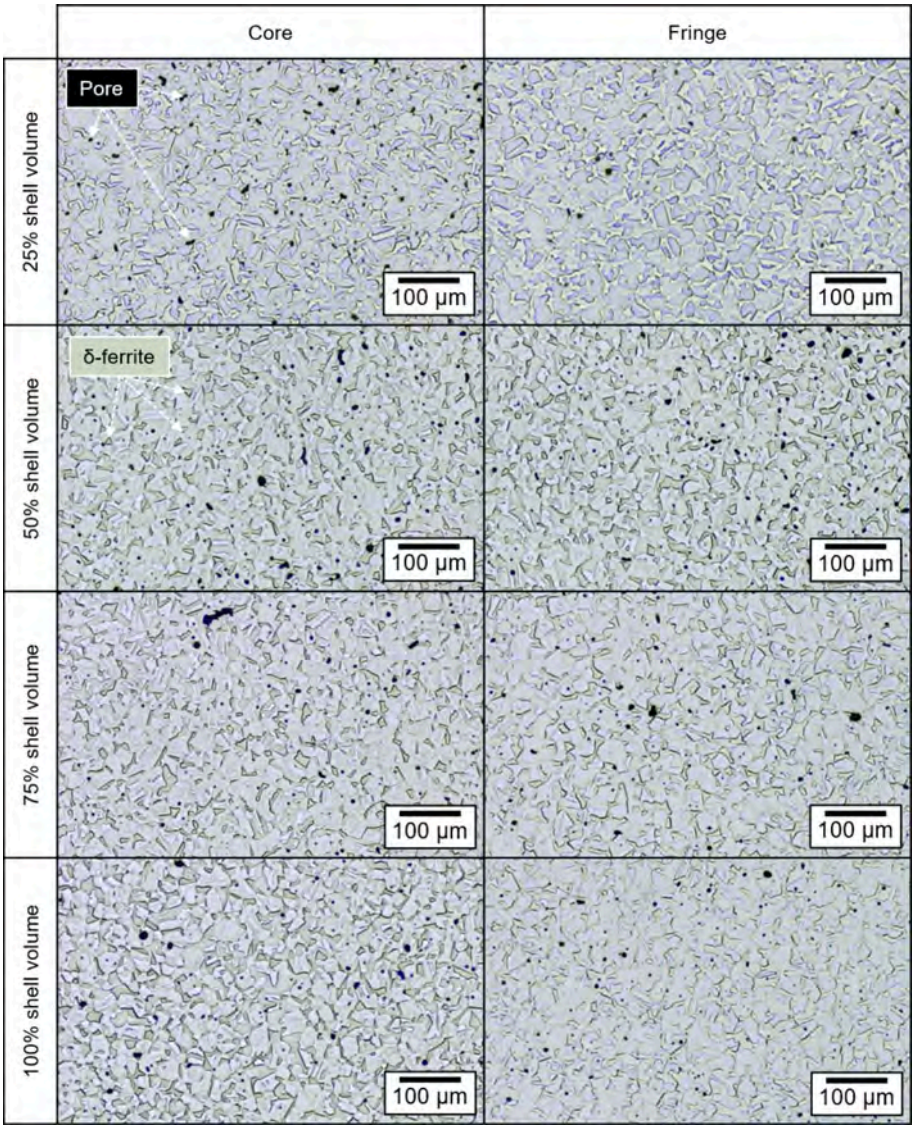

Fig. 13. Microstructure at the core and fringe of the samples sintered in H_2 for 25%, 50%, 75% and 100% shell volume.

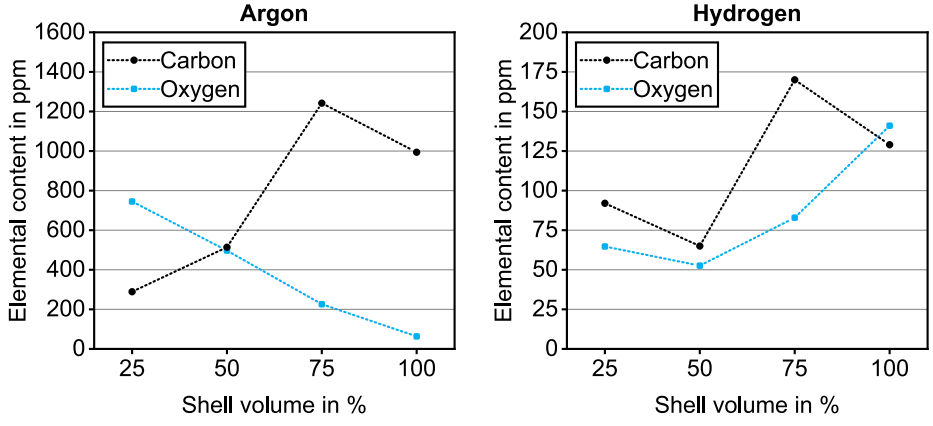

Fig. 14. Carbon and oxygen contents of samples sintered in Ar and H_2 depending on the printed shell volume.

that used in Fig. 16 in order to more effectively illustrate the gradients, as the porosity values in the present case are substantially lower. For 25% shell volume, the center showed a high porosity of ~0.15%, whereas the surrounding porosity values were below 0.05% except for one outlier. For 25% shell volume, most of the pore diameters in the core of the samples were below 3 µm, while bigger pore diameters were found towards the fringe of the cross-section. The microhardness showed no notable gradient with a mean value of 293 ± 13 HV0.1.

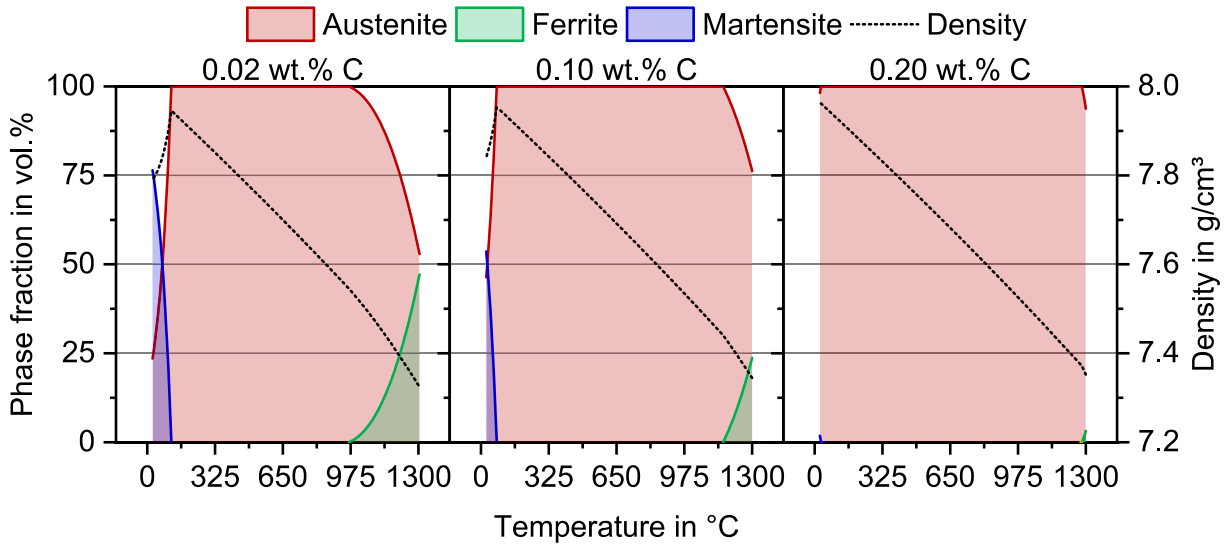

Fig. 15. Phase fractions of austenite, ferrite and martensite during cooling of 17-4 PH stainless steel for 0.02 wt%, 0.10 wt% and 0.20 wt% carbon calculated by JMatPro.

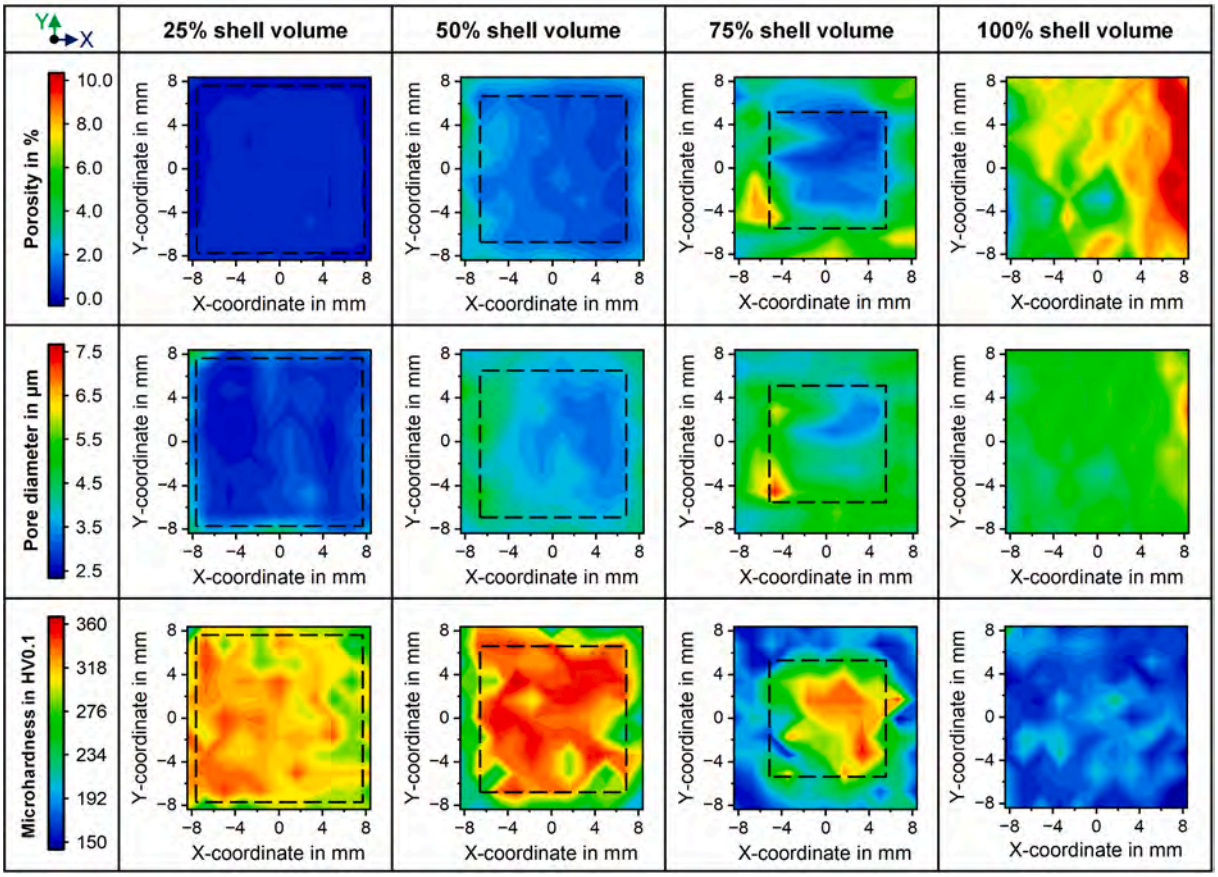

Fig. 16. Distribution of porosity, equivalent pore diameter and microhardness in the XY-plane for 25%, 50%, 75% and 100% shell volume sintered in Ar.

For 50% shell volume, the area of increased porosity in the center reduced compared to 25% shell volume, while the surrounding porosity of ~0.17% was comparable. Overall, the porosity gradient was the lowest for 50% shell volume. The pore diameters for 50% shell volume were comparable to 25% shell volume. Some areas of increased hardness were found for 50% shell volume. The mean value remained comparable at 297 ± 15 HV0.1 to 25% shell volume.

An area of increased porosity was identified for 75%, which was aligned towards the left side facing the pushrod in X-direction. The sample shell with 75% shell volume demonstrated notably higher pore diameters of ~5.2 µm than the core region of ~3.6 µm. The core exhibited higher microhardness values than the shell. The mean value was 305 ± 18 HV0.1.

For 100% shell volume, a higher porosity and larger pore diameters

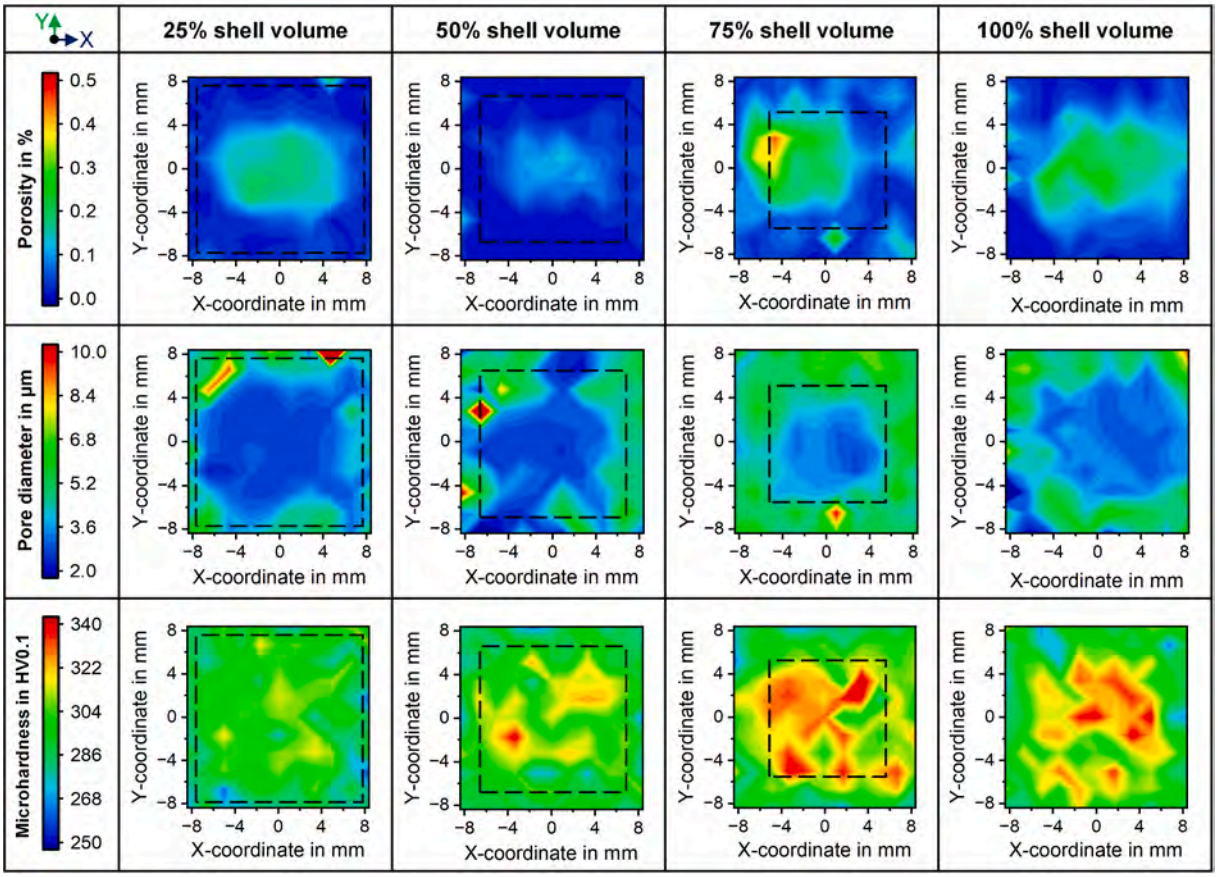

Fig. 17. Distribution of porosity, equivalent pore diameter and microhardness in the XY-plane for 25%, 50%, 75% and 100% shell volume sintered in H_2.

were present at the core of the sample than at the fringe of the sample. The microhardness increased in the core of the sample compared to the fringe. The mean microhardness value of 303 ± 18 HV0.1 was similar to 75% shell volume.

3.3.1. *Phase fractions of core and shell*

Fig. 18 highlights the fractions of austenite (fcc) obtained from EBSD mappings along with the grain orientation for 25% and 100% shell volume sintered in Ar from the fringe to the core of the samples. The fraction of retained austenite (fcc) is below 0.5% for 25% shell volume, while a significant fraction is present in the sample with 100% shell volume. The fraction of retained austenite (fcc) in the fringe was 68%, while 39% in the core for 100% shell volume. The fraction of δ-ferrite decreased slightly from ~7% at the fringe to ~5% in the core for 25% shell volume. The corresponding size of the δ-ferrite grains decreased from ~41 µm in the fringe to ~22 µm in the core. No preferential grain orientation is evident, which is common for sintered steels.

Fig. 19 depicts the EBSD mappings for 25% and 100% shell volume from the fringe to the core of samples sintered in H_2. There were negligible fractions of retained austenite below 0.5% for 25% and 100% shell volume. The microstructure mainly consisted of martensite and δ-ferrite distributed along prior austenite grain boundaries. For 25% shell volume, the δ-ferrite fraction declined from ~15% in the fringe to ~9% in the core, while the grain sizes of δ-ferrite decreased from ~78 µm to ~41 µm. In the case of 100% shell volume, the δ-ferrite fraction reduced slightly from ~7% in the fringe to ~6% in the core, but the corresponding grain sizes decreased notably from ~56 µm to ~33 µm.

4. Discussion

4.1. *Influence of binder on green density*

The calculation of the binder mass demonstrated that it has a low impact on the green part's mass and density. Consequently, the significant increase of the green sample mass by ~0.29 g from 25% to 100% shell volume originated primarily from an increased powder mass since the binder mass increased only by ~0.04 g. The green density increased nearly linearly with the shell volume. The linearity between shell volume and green density suggests that the powder packing was higher in the shell than in the core of each sample. Consequently, the increased powder packing must be connected to the powder-binder interaction in the shell area during printing. It is suspected that the dotted binder printing pattern shown in Fig. 1 might also lead to variations in powder packing on a micro-scale, but this could not be observed in the sintered microstructure.

It is argued that the binder can improve particle rearrangement during printing [10,21]. The deposited liquid binder covers the particles, penetrates into the powder bed and is forced into the necks between the particles by capillary pressure [21]. The liquid will reduce its surface-to-volume ratio and decrease the liquid-vapor interface area to minimize the surface energy [21]. Therefore, the particles rearrange due to the surface tension of the liquid. In addition, the interaction of the powder with the compaction roller might be influenced by the presence of binder on the powder bed.

Miao et al. [10] proposed an equation to describe the green density for shell-printed samples with the shell density ρ_S, core density ρ_C and the shell volume fraction f_S. In the current study, the linear extrapolation of the green density to 0% shell volume would approximate a core density of 4.34 g/cm^3 unaffected by the binder. The shell density is

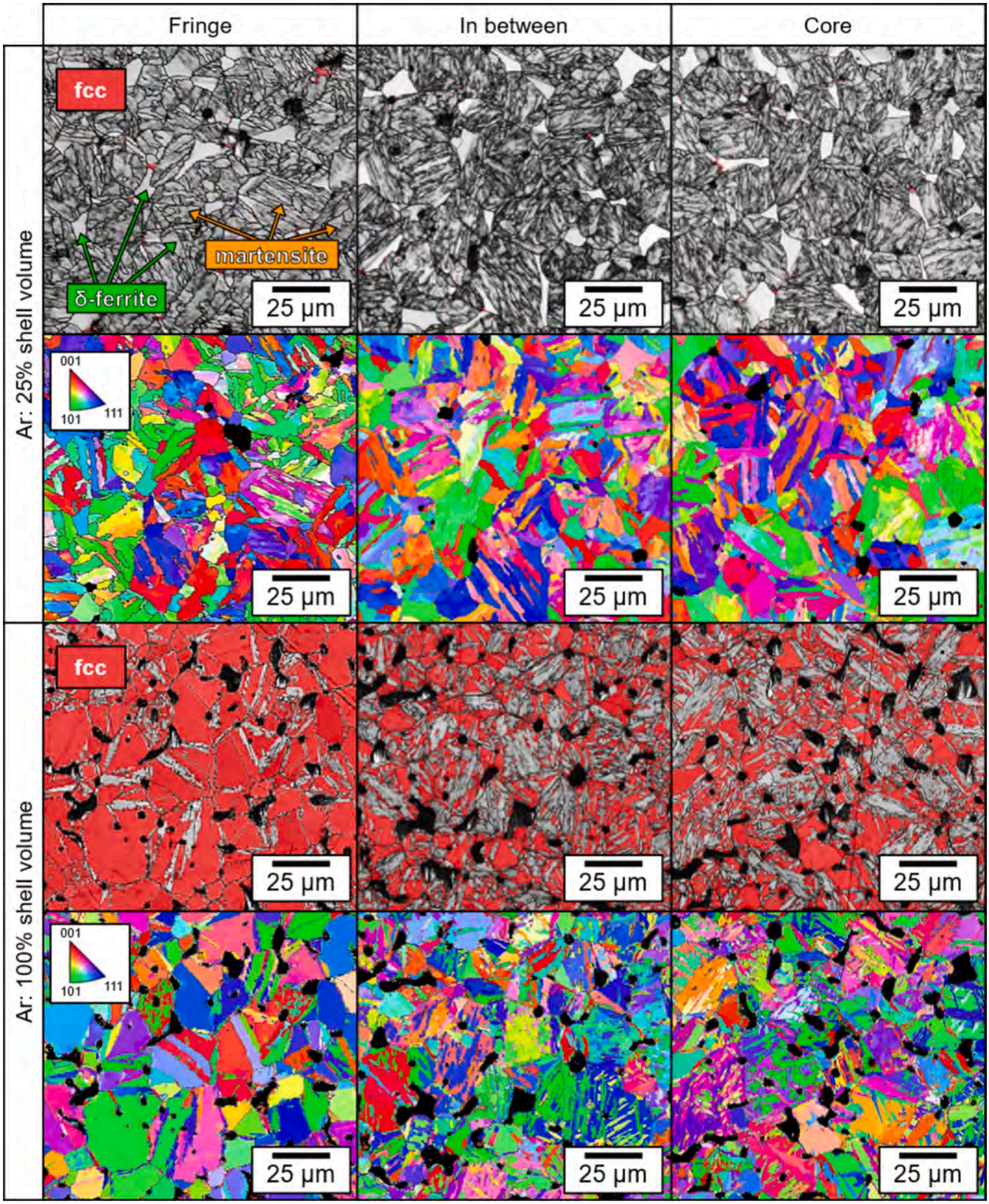

Fig. 18. EBSD band contrast maps in the first and third row with overlayed fcc phases (in red) along with EBSD orientation maps in the second and fourth row for 25% and 100% shell volume sintered in Ar from the fringe to the core region. (For interpretation of the references to colour in this figure legend, the reader is referred to the web version of this article.)

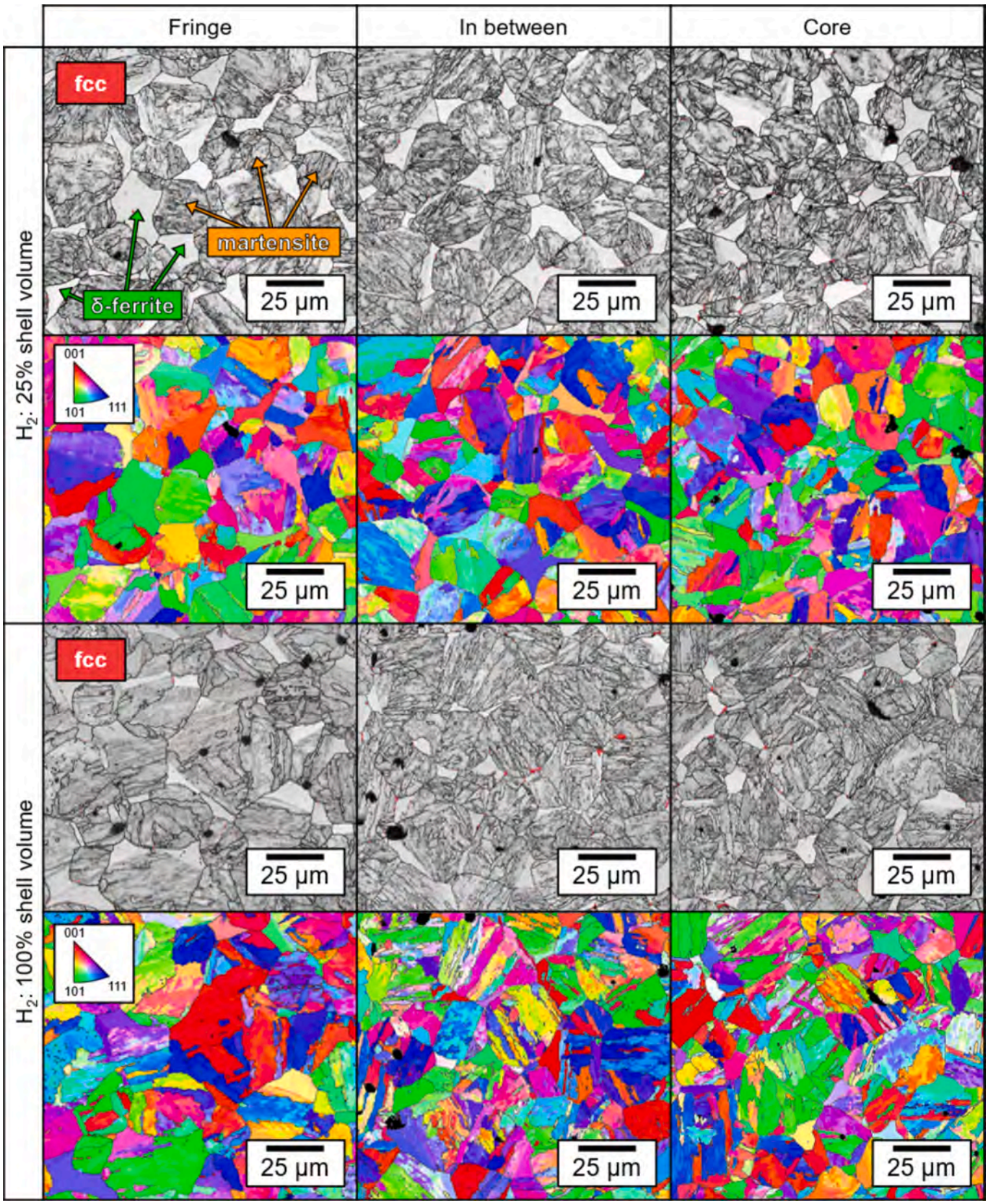

Fig. 19. EBSD band contrast maps in the first and third row with overlayed fcc phases (in red) along with EBSD orientation maps in the second and fourth row for 25% and 100% shell volume sintered in H_2 from the fringe to the core region. (For interpretation of the references to colour in this figure legend, the reader is referred to the web version of this article.)

assumed to be the density of the sample with 100% wall volume, which was 4.84 g/cm^3. Thus, the green density of the 17-4 PH samples printed in this study can be expressed for varying shell volumes by the following equation:

$$\rho = \rho_S f_S + \rho_C (1 - f_S) = 4.84 \frac{g}{cm^3} f_S + 4.34 \frac{g}{cm^3} (1 - f_S)$$

The green density of the shell was 11.5% higher than in the core. The relative green density increased from 55.5% to 61.9%, based on the powder density of 7.82 g/cm^3. Miao et al. [10] revealed via CT images for alumina powder that the relative green density increased by 3.7% in the shell for D_{50} = 10 μm and 2.1% for D_{50} = 23 μm compared to the core. Huang et al. [22] demonstrated for zirconia ceramics that a higher binder saturation increased the green density for polyvinyl pyrrolidone and inorganic binders, which was explained by the binder causing local particle rearrangement.

Most studies reported, however, a detrimental impact of the binder on the powder packing [8,9,23,24]. The contradicting findings in the literature and in this study lead to the conclusion that the effect of the binder on powder packing depends on several factors. These factors include the powder characteristics, the binder composition, the binder-powder interaction (directly correlated to the previous two parameters), the printer hardware and printing parameters. The printer hardware used in this study differs from most commercially available printers since the powder and binder are deposited in a single pass. Furthermore, the powder bed is steamed before binder deposition to increase powder cohesion in order to prevent powder ejecta.

Generally, a higher powder packing in the green part is favored since close neighbors build new contacts to increase the coordination number [25,26]. The sintered density increases as the initial coordination number increases [25,27]. Barthel et al. [28] showed that a high green density led to a high sintered density for 316L stainless steel powder, which was explained by the increased contact points between particles for higher green densities. In addition, a higher powder packing requires less shrinkage to achieve full densification [24,29], which makes dimensional control less challenging.

4.2. Impact of green density and binder content on sintering densification

The powder characteristics can be assumed to be identical for all samples, as they were printed in the same build job. However, as discussed in the previous section, the initial binder content and powder packing in the green parts varied for the different shell volumes, which resulted in different sintering shrinkages during dilatometry.

For both processing atmospheres, the sintering onset temperature rose with increasing shell volume since increasing powder packing reduces the thermodynamic driving force of sintering connected to the free surface energy [30,31]. In addition, a higher binder content and powder packing are assumed to slow down the removal of debinding products and the penetration of processing gas due to lower open porosity. This, in turn, hinders sintering neck formation.

Considerable differences were found between sintering in H_2 and Ar. For sintering in H_2, nearly full densification was obtained for 25%, 50%, 75% and 100% shell volume. The shrinkage increased with decreasing shell volume, compensating for the lower green densities. A high powder packing made dimensional control less challenging due to lower shrinkage. For processing in Ar, the sintering shrinkage decreased from 25% to 100% shell volume but much more significantly than for H_2. Consequently, the sintered densities notably reduced from 25% to 100% shell volume, although the powder packing increased.

Despite increasing binder content, processing in H_2 allowed for sufficient binder removal for all shell volumes. The H_2 can aid the decomposition of the binder and is efficient in removing carbon [2]. The sintered carbon contents were slightly below the virgin powder content, which suggested that carbon stemming from the powder was consumed for the reduction of metal oxides [15,32]. The sintered oxygen content dropped notably below 150 ppm compared to the 1163 ppm of the virgin powder, which is attributed to the reducing effect of H_2 [33–35]. The sintered oxygen content increased with the shell volume, which can be linked to the increased powder packing, higher powder mass and hence lower gas penetration.

In contrast, binder removal was less efficient for processing in inert Ar, as no reactive species were provided to aid binder decomposition [4]. The carbon contents after sintering were higher compared to the virgin powder, indicating the presence of binder residues. The binder removal was still sufficient for 25% shell volume, as the sintered carbon content was slightly higher than the virgin powder. However, the debinding became increasingly insufficient with increasing shell volume, which resulted in notable carbon pickup after sintering.

The sintered oxygen content for processing in Ar was lower than for the virgin powder, which can be attributed to the carbothermal reduction of metal oxides by carbon during sintering [15,36]. Furthermore, the sintered oxygen content decreased with increasing shell volume, which is linked to the increased binder content and, thereby, carbon availability for carbothermal reduction. While the sintered oxygen content decreased from 25% shell volume to 100% shell volume for sintering in Ar, the sintered densities decreased. Since improved oxide removal would generally be expected to enhance sintering densification, the obtained densities indicate that oxide reduction is not the primary factor limiting the sintering densification under Ar atmosphere.

The largest difference in sintered densities between Ar and H_2 was measured for the samples with 100% shell volume, despite comparable low sintered oxygen contents. Furthermore, the sample with 25% shell volume achieved higher sintered densities under Ar despite exhibiting significantly lower green density than the sample with 100% shell volume. If sintering densification was primarily controlled by initial powder packing density or oxide reduction, the opposite trend in sintered densities would be expected.

The reason for the deviation in the sintering densification can be understood by analyzing the as-sintered microstructure. After sintering in H_2, the presence of island-type δ-ferrite was observed at prior austenite grain boundaries, which was not the case after sintering in Ar. The δ-ferrite phase is commonly observed in sintered 17-4 PH stainless steel [6,14]. The δ-ferrite phase enhances the sintering densification in comparison to the γ-austenite matrix since the self-diffusivity in the bcc crystal structure of δ-ferrite is higher than that in the fcc crystal structure of γ-austenite [5,37].

The formation of δ-ferrite was registered during dilatometry for H_2 sintering by a rapid increase in the shrinkage rate above 1150°C. According to thermodynamic simulations, a high fraction of δ-ferrite (49 vol%) during sintering was predicted for 200 ppm of carbon. In contrast, the formation of δ-ferrite was only slightly indicated at 1290°C for sintering in Ar. The lack of δ-ferrite can be attributed to the high residual carbon content of ~1000 ppm for 100% shell volume after sintering in Ar. Carbon is a strong austenite stabilizer and hinders the formation of δ-ferrite during sintering [38]. The thermodynamic calculations showed that a low δ-ferrite fraction of 3 vol% at 1300°C was expected for 0.20 wt % (2000 ppm) of carbon. The carbon content during heating is expected to be higher than the sintered carbon content. Chang et al. [39] demonstrated for injection molded 17-4 PH stainless steel that an increased carbon content decreases the fraction of δ-ferrite in the microstructure.

For 100% shell volume, the microhardness for sintering in Ar was significantly lower than after sintering in H_2, which was also connected to the carbon content. 17-4 PH stainless steel typically forms martensite upon cooling [38], which is affected by the carbon content. The martensitic transformation was predicted at ~115°C for 200 ppm of carbon, which is accompanied by a volume expansion and hence density decrease.

During cooling, a linear expansion associated with martensitic transformation was measured starting at around 162°C for all samples sintered in H_2, whereas no apparent expansion was observed for the

100% shell volume sample sintered in Ar. This observation is consistent with the measured microhardness values, where high hardness values were obtained for samples sintered in H_2 and significantly lower values for the 100% shell volume sample sintered in Ar. The expansion behavior is further supported by the phase fractions determined via EBSD. For samples sintered in H_2 (25% and 100% shell volume) as well as for the sample with 25% shell volume sintered in Ar, retained austenite fractions (fcc) were negligible below 0.5%. EBSD analysis indicated that the microstructure predominantly consisted of bcc phases with martensitic structures and island-type δ-ferrite.

In contrast, high fractions of retained austenite (fcc) up to 68% were measured by EBSD for the 100% shell volume sample sintered in Ar, in accordance with low microhardness values and no linear expansion during cooling after sintering. The high carbon content shifted the martensitic transformation for a high fraction of austenite grains to temperatures below room temperature, as carbon lowers the martensitic transformation temperatures [38,40–42].

The powder packing was assumed to be consistent across the sample with 100% shell volume, as no binder-free core region with lower green density was present. Nevertheless, an apparent area of increased porosity and microhardness was revealed in the center compared to the fringe of the sample after sintering in H_2. Consequently, the gradient is presumed to be connected to a debinding gradient. It is hypothesized that a lower debinding activity in the core of the sample results in higher carbon content during sintering, inhibiting the formation of δ-ferrite in the core. EBSD analysis suggested that the fraction of δ-ferrite was slightly larger in the fringe than in the core of the sample with 100% shell volume sintered in H_2, supporting the claim.

Coarser grains at the fringe compared to the core after sintering in H_2 could be connected to the debinding gradient described in the previous paragraph, but also to a faster and more efficient removal of oxides at the surface of the part, since oxides hinder grain growth by grain boundary pinning. Another potential influence could be temperature gradients from the surface to the core of the part during sintering. In addition, the powder packing and initial contact points between powder particles influence the number of initial grains and the subsequent grain growth during sintering.

A lower fraction of δ-ferrite in the core, as suggested by EBSD measurements, would explain higher porosity in the core compared to the shell. Consequently, a higher fraction of martensitic phases and carbon would be present in the core compared to the fringe, leading to higher microhardness in the core. A similar gradient in porosity and microhardness was observed for 75% shell volume sintered in H_2. The potential debinding gradient led to higher sintered porosity for 100% and 75% shell volume compared to 25% and 50% shell volume, although the initial green densities were higher for 75% and 100% shell volume.

Huber et al. [43] reported for BJT of 17-4 PH that δ-ferrite fractions were 1.5 to 15 times higher in the fringe than the core of a bulk sample, which might be due to differences in carbon content between the core and fringe. In addition, the hardness increased in the core of the sample [43], similar to the findings of this study.

For 100% shell volume sintered in Ar, no apparent gradient in the microhardness and pore diameters was notable. Only the porosity increased in the X-direction away from the pushrod, which can be connected to a debinding gradient due to the gas flow direction. Interestingly, the pore diameters for 100% shell volume were similar to the shell regions of 50% and 75% shell volume, despite severe differences in the overall sintering densification under Ar atmosphere. One potential reason could be the binder expansion and evaporation during debinding, creating large pores. Another potential reason might be the ballistic effect of the binder inducing a few larger pores during printing [12,13], increasing the mean pore diameters in the shell despite lower overall porosity.

The most significant microstructure gradients were revealed for 75% shell volume sintered in Ar. The core region exhibited lower porosity than the shell region, which was separated by the core–shell interface. The lower porosity in the core was due to the presence of δ-ferrite in the microstructure, while no δ-ferrite was observed in the shell. The formation of δ-ferrite in the core was registered during dilatometry by the more pronounced increase in the shrinkage rate compared to 100% shell volume. The carbon residue from the binder prevented the formation of δ-ferrite in the shell, resulting in lower densification during sintering. Mariani et al. [11] observed a similar behavior for 316L stainless steel, where carbon residue had a detrimental impact on the formation of δ-ferrite in the shell, leading to less densification.

The porosity gradient for 75% shell volume sintered in Ar was accompanied by a large microhardness gradient, where high values above 300 HV0.1 in the core indicated martensite formation in contrast to values below 200 HV0.1 in the shell, where a high fraction of retained austenite is expected. The macrohardness of BJT 17-4 PH typically exhibits values above 300 HV10 [43–45]. The low hardness in the binder-affected shell implies less martensite formation and higher fractions of retained austenite due to high carbon content, which is supported by the absence of δ-ferrite in the shell.

The porosity for 50% shell volume sintered in Ar decreased notably compared to 75% shell volume since a lower carbon residue resulted in a higher fraction of δ-ferrite during sintering, as confirmed by a higher shrinkage rate peak during dilatometry compared to 50% shell volume. The fraction of δ-ferrite was higher in the core than in the fringe of the sample, which resulted in higher densification in the core. The microhardness showed an apparent increase above 300 HV0.1 in the binder-free core region compared to the shell region. This indicated martensite formation in the core, as implied by a rapid expansion at 79°C during dilatometry.

For 25% shell volume sintered in Ar, the sintering shrinkage increased significantly compared to 50% shell volume, which was close to sintering in H_2 for 25% shell volume. The high fractions of δ-ferrite were in accordance with the lower carbon content of 289 ppm after sintering in Ar for 25% shell volume. However, the fraction and sizes of δ-ferrite were still notably lower compared to 25% shell volume sintered in H_2 owing to the lower debinding activity in Ar. The bulk density for the sample sintered in Ar was ~0.2 g/cm^3 lower than for H_2, although the porosity was only slightly higher. This could be linked to the differences in the phase compositions as observed for EBSD.

For 25% shell volume sintered in Ar, the porosity increased slightly in the core of the sample compared to the shell, while the pore diameters showed a reverse trend. As no binder inhibited δ-ferrite formation in the core, the higher porosity is connected to the lower initial powder packing in the core. The larger pore diameters in the shell, despite lower porosity, are probably linked to the ballistic effect of the binder, ejecting particles from the powder bed [12,13]. The hardness showed a slight decline in the X-direction away from the pushrod, which could be connected to the direction of the gas stream. Nevertheless, an evident expansion connected to martensite formation was confirmed by dilatometry at 119°C, which was at a higher temperature than for 25% shell volume due to the lower carbon content.

The lowest gradients in porosity, pore diameters and microhardness were measured for 25% and 50% shell volume sintered in H_2. No noticeable gradient in the microhardness was observed for 25% shell volume. However, a slight gradient of increased porosity in the center of the cross-section was evident. The pore diameters were lower in the core and increased towards the sample shell. The higher porosity in the core is likely connected to the lower powder packing. At the same time, the higher pore diameters in the shell are assumed to be caused by the ballistic binder effect during printing [12,13]. Another potential reason could be the binder expansion and evaporation during debinding, which can create larger pores.

The sample with 50% shell volume sintered in H_2 led to the lowest porosity gradients, while an apparent pore diameter difference was notable between the core and shell. Some random areas of increased microhardness were measured in the core area, which could be linked to fluctuations in the martensite and ferrite phase fractions. Sintering of

50% shell volume in H_2 appeared to strike the best balance between improved powder packing by the binder while minimizing debinding gradients and, thereby, carbon gradients during sintering. The difference in the powder packing might also affect the potential nucleation sites of δ-ferrite, which preferentially nucleates along grain boundaries due to the lower nucleation barrier at grain boundaries [5,46].

The insights presented in this study are based on a simple geometry with a single size. It is suspected that the part size and geometry will have a significant effect on the shell printing strategy. In particular, the ratio of shell thickness to overall part size may affect the extent of the observed gradients. Furthermore, the impact of the binder may vary within a single component with varying wall thicknesses and feature sizes. In addition, the green strength must be considered for larger components, as the shell structure of the green part must support the weight of the enclosed loose powder during handling and subsequent thermal processing.

5. Conclusions

This study highlighted the influence of the binder on powder packing, sintering densification, phase transformations and microstructure gradients of 17-4 PH stainless steel by utilizing the shell printing strategy for BJT, which divides the green parts into a binder-free core and a binder-affected shell. The sintering of green samples with 25%, 50%, 75% and 100% shell volume in a dilatometer under H_2 and Ar atmosphere demonstrated the opposing effects of powder packing and binder contamination on the sintering densification. The main insights of the study are the following:

- The increase of the shell volume resulted in a significant rise of the green density from 4.46 g/cm^3 for 25% shell volume to 4.82 g/cm^3 for 100% shell volume. This increase by 0.36 g/cm^3 was mainly due to a higher powder packing, as the binder mass accounted only for ~11% of the density increase. The improved green density was attributed to the binder-induced particle rearrangement during printing. The density was expected to be 4.82 g/cm^3 in the shell (100% shell volume), while a density of 4.34 g/cm^3 was predicted for the core by linear extrapolation (0% shell volume).
- Sintering in H_2 was mainly dominated by the differences in powder packing. The declining green densities with decreasing shell volume were compensated by higher sintering shrinkages, leading to comparable densities ranging from 99.7% to 99.9%. Low sintered carbon and oxygen contents indicated efficient binder and metal oxide removal for H_2 processing. Microhardness values around 300 HV0.1 confirmed martensite formation.
- After sintering in H_2, minor debinding gradients were detected for 75% and 100% shell volume, with higher porosity and microhardness in the core than in the shell. This was attributed to the higher carbon content in the core, slightly reducing the δ-ferrite fraction, inhibiting sintering densification and increasing the martensite fraction after cooling. For 25% and 50% shell volume, the core exhibited higher porosity than the shell, which was linked to the lower initial powder packing in the core compared to the shell. At the same time, the shell exhibited larger pores than the core, which could be connected to binder expansion and evaporation during debinding or the ballistic effect of the binder during printing, causing larger pores in the shell.
- Sintering in Ar was detrimentally impacted by carbon introduced by the binder due to the low debinding activity, which affected the phase transformations of 17-4 PH. Increasing shell volumes resulted in higher binder residuals and, thereby, sintered carbon content, which reduced the formation of δ-ferrite required for high sintering densification. Consequently, the sintered densities declined significantly from 99.3% for 25% shell volume to 93.4% for 100% shell volume. However, the sintered oxygen decreased with increasing shell volume since the carbon availability for carbothermal reduction increased.
- After sintering in Ar, no δ-ferrite was observed in the as-sintered microstructure for 100% shell volume due to the carbon contamination, leading to high porosity. The increased carbon content led to retained austenite in the sintered microstructure with fractions of up to 68%, resulting in microhardness values below 200 HV0.1. Significant porosity and microhardness gradients were found for 75% and 50% shell volume since carbon contamination in the shell prevented the formation of δ-ferrite and stabilized austenite during cooling. The core regions, however, showed δ-ferrite phases and a high microhardness, indicating high martensite fractions. For 25% shell volume, the processing in Ar allowed for sufficient binder removal, resulting in a high sintered density of 99.3% in combination with a mean microhardness above 300 HV0.1 due to martensite formation upon cooling.

If the processing atmosphere ensures efficient debinding, the detrimental impact of the binder can be mostly negated while slight microstructure gradients remain. If the processing atmosphere leads to inefficient debinding, the shell printing approach can provide a successful strategy to reduce the detrimental impact of the binder and lower the requirements on the debinding process, such as atmosphere and time. However, the risk of significant microstructure gradients rises with shell printing.

CRediT authorship contribution statement

Kai Zissel: Writing – original draft, Visualization, Validation, Methodology, Investigation, Formal analysis, Data curation, Conceptualization. **Gowtham Soundarapandiyan:** Writing – review & editing, Visualization, Validation, Investigation, Formal analysis. **Sophie Dubiez-Le Goff:** Writing – review & editing, Validation, Supervision, Resources, Conceptualization. **Eduard Hryha:** Writing – review & editing, Validation, Supervision, Methodology, Funding acquisition.

Declaration of competing interest

The authors declare that they have no known competing financial interests or personal relationships that could have appeared to influence the work reported in this paper.

Acknowledgments

This work was conducted in the framework of the Centre for Additive Manufacturing – Metal (CAM^2), supported by the Swedish Governmental Agency of Innovation Systems (Vinnova). Linde GmbH acknowledges the funding by the Federal Ministry of Research and Education (BMBF, Germany) for the project SINEWAVE (FKZ 03HY123A) within the Hydrogen Flagship Project H2Giga.

Data availability

Data will be made available on request.

References

[1] ISO/ASTM 52900:2021 Additive manufacturing – General principles – Fundamentals and vocabulary, (2021).
[2] R.M. German, A. Bose, Binder Removal, in: Bind. Polym. Assist. Powder Process.,, ASM International, 2020, pp. 139–167, 10.31399/asm.tb.bpapp.t59290139.
[3] R.K. Enneti, S.J. Park, R.M. German, S.V. Atre, Review: thermal debinding process in particulate materials processing, Mater. Manuf. Process. 27 (2012) 103–118, https://doi.org/10.1080/10426914.2011.560233.
[4] K. Zissel, E. Bernardo, P. Forêt, E. Hryha, Impact of oxygen content on debinding of binder jetted 17-4 PH stainless steel: Part I – Debinding, Powder Metall. 68 (2024) 3–15, https://doi.org/10.1177/00325899241307824.

[5] Y. Wu, D. Blaine, B. Marx, C. Schlaefer, Effects of residual carbon content on sintering shrinkage, microstructure and mechanical properties of injection molded 17-4 PH stainless steel, J. Mater. Sci. 37 (2002) 3573–3583, https://doi.org/10.1023/A:1016532418920.
[6] R.M. German, MIM 17-4 PH Stainless Steel: Processing, properties and best practice, Powder Inject. Mould. Int. 12 (2018) 49–76.
[7] R. Frykholm, Y. Takeda, B.-G. Andersson, R. Carlström, Solid State Sintered 3-D Printing Component by using Inkjet (Binder) Method, J. Jpn. Soc. Powder Powder Metall. 63 (2016) 421–426, https://doi.org/10.2497/jjspm.63.421.
[8] M. Khademitab, M. Jamalkhani, K. Bishaj, E. Jenssen, M. Heim, D. Nelson, N. M. O'Dowd, A. Mostafaei, Does selective shell printing advance binder jetting additive manufacturing? Powder Technol. 441 (2024) 119812 https://doi.org/10.1016/j.powtec.2024.119812.
[9] K.M. Rahman, A. Wei, H. Miyanaji, C.B. Williams, Impact of binder on part densification: Enhancing binder jetting part properties through the fabrication of shelled geometries, Addit. Manuf. 62 (2023) 103377, https://doi.org/10.1016/j.addma.2022.103377.
[10] G. Miao, M. Moghadasi, M. Li, Z. Pei, C. Ma, Binder Jetting Additive Manufacturing: Powder Packing in Shell Printing, J. Manuf. Mater. Process. 7 (2023) 4, https://doi.org/10.3390/jmmp7010004.
[11] M. Mariani, L. Montipò, N. Lecis, Effects of feedstock morphology and composition on binder jetting of 316L stainless steel: a perspective on circular economy. Euro PM2023 Proc, European Powder Metallurgy Association (EPMA), Lisbon, Portugal, 2023.
[12] N.D. Parab, J.E. Barnes, C. Zhao, R.W. Cunningham, K. Fezzaa, A.D. Rollett, T. Sun, Real time observation of binder jetting printing process using high-speed X-ray imaging, Sci. Rep. 9 (2019) 2499, https://doi.org/10.1038/s41598-019-38862-7.
[13] J.E. Lawrence, M.P. Lawrence, K. Fezzaa, S.J. Clark, N.B. Crane, High-speed X-ray imaging of droplet-powder interaction in binder jet additive manufacturing, Addit. Manuf. 89 (2024) 104269, https://doi.org/10.1016/j.addma.2024.104269.
[14] R.M. German, A. Bose, Case studies of powder-binder processing practices, in: Bind. Polym. Assist. Powder Process., ASM International, 2020, pp. 201–249, 10.31399/asm.tb.bpapp.t59290201.
[15] K. Zissel, E. Bernardo, P. Forêt, E. Hryha, Impact of oxygen content on debinding of binder jetted 17-4 PH stainless steel: Part II – Sintering, Powder Metall. 68 (2024) 16–28, https://doi.org/10.1177/00325899241307871.
[16] Metal Powder Industries Federation, MPIF STANDARD 35 - STRUCTURAL PARTS, 2018.
[17] B09 Committee, Standard Specification for Metal Injection Molded (MIM) Materials, ASTM B883-24, n.d. https://www.astm.org/b0883-24.html.
[18] A. Cabo Rios, E. Hryha, E. Olevsky, P. Harlin, Sintering anisotropy of binder jetted 316L stainless steel: part II – microstructure evolution during sintering, Powder Metall. (2022) 1–13, https://doi.org/10.1080/00325899.2021.2020486.
[19] A. Cabo Rios, E. Hryha, E. Olevsky, P. Harlin, Sintering anisotropy of binder jetted 316L stainless steel: part I – sintering anisotropy, Powder Metall. (2021) 1–10, https://doi.org/10.1080/00325899.2021.2020485.
[20] A. Cabo Rios, T. Mishurova, L. Cordova, M. Persson, G. Bruno, E. Olevsky, E. Hryha, Ex-situ characterization and simulation of density fluctuations evolution during sintering of binder jetted 316L, Mater. Des. 238 (2024) 112690, https://doi.org/10.1016/j.matdes.2024.112690.
[21] M.J. Cima, A. Lauder, S. Khanuja, E. Sachs, Microstructural elements of components derived from 3D printing, in: Proc. 1992 Int. Solid Free. Fabr. Symp., 1992, pp. 220–227, 10.15781/T2W37MC63.
[22] S. Huang, C. Ye, H. Zhao, Z. Fan, Q. Wei, Binder jetting yttria stabilised zirconia ceramic with inorganic colloid as a binder, Adv. Appl. Ceram. 118 (2019) 458–465, https://doi.org/10.1080/17436753.2019.1666593.
[23] M. Li, G. Miao, W. Du, Z. Pei, C. Ma, Difference between powder bed density and green density for a free-flowing powder in binder jetting additive manufacturing, J. Manuf. Process. 84 (2022) 448–456, https://doi.org/10.1016/j.jmapro.2022.10.030.
[24] B.J. Paudel, A.C. To, Spatial green density variation and its effect on distortion prediction in binder jet additive manufacturing, Addit. Manuf. 98 (2025) 104640, https://doi.org/10.1016/j.addma.2025.104640.
[25] R.M. German, Coordination number changes during powder densification, Powder Technol. 253 (2014) 368–376, https://doi.org/10.1016/j.powtec.2013.12.006.
[26] E. Stevens, S. Schloder, E. Bono, D. Schmidt, M. Chmielus, Density variation in binder jetting 3D-printed and sintered Ti-6Al-4V, Addit. Manuf. 22 (2018) 746–752, https://doi.org/10.1016/j.addma.2018.06.017.
[27] T. Rasp, T. Kraft, H. Riedel, Discrete element study on the influence of initial coordination numbers on sintering behaviour, Scr. Mater. 69 (2013) 805–808, https://doi.org/10.1016/j.scriptamat.2013.09.003.
[28] B. Barthel, F. Janas, S. Wieland, Powder condition and spreading parameter impact on green and sintered density in metal binder jetting, Powder Metall. 64 (2021) 378–386, https://doi.org/10.1080/00325899.2021.1912923.
[29] M.N. Rahaman, Sintering theory and fundamentals, in: P. Samal, J. Newkirk (Eds.), Powder Metall., ASM International, 2015, pp. 205–236, https://doi.org/10.31399/asm.hb.v07.a0006117.
[30] S. Baselli, A. Molinari, A dilatometry study of the influence of green density on anisothermal and isothermal shrinkage of plain iron green parts, Powder Metall. 63 (2020) 155–162, https://doi.org/10.1080/00325899.2020.1777723.
[31] A. Molinari, S. Amirabdollahian, M. Zago, M. Larsson, I. Cristofolini, Effect of geometry and green density on the anisotropic sintering shrinkage of axisymmetric iron parts, Powder Metall. 61 (2018) 267–275, https://doi.org/10.1080/00325899.2018.1483064.
[32] R. de Oro Calderon, M. Jaliliziyaeian, C. Gierl-Mayer, H. Danninger, Effects of H2 atmospheres on sintering of low alloy steels containing oxygen-sensitive masteralloys, JOM 69 (2017) 635–644, https://doi.org/10.1007/s11837-017-2287-9.
[33] E. Hryha, L. Nyborg, Thermogravimetry study of the effectiveness of different reducing agents during sintering of Cr-prealloyed PM steels, J. Therm. Anal. Calorim. 118 (2014) 825–834, https://doi.org/10.1007/s10973-014-3915-z.
[34] R. Oro, M. Campos, C. Gierl-Mayer, H. Danninger, J.M. Torralba, New Alloying Systems for Sintered Steels: critical Aspects of Sintering Behavior, Metall. Mater. Trans. A 46 (2015) 1349–1359, https://doi.org/10.1007/s11661-014-2707-1.
[35] R. De Oro Calderon, C. Gierl-Mayer, H. Danninger, Application of thermal analysis techniques to study the oxidation/reduction phenomena during sintering of steels containing oxygen-sensitive alloying elements, J. Therm. Anal. Calorim. 127 (2016) 91–105, https://doi.org/10.1007/s10973-016-5508-5.
[36] C. Gierl-Mayer, Reactions between ferrous powder compacts and atmospheres during sintering – an overview, Powder Metall. 63 (2020) 237–253, https://doi.org/10.1080/00325899.2020.1810427.
[37] X. Xu, J. Li, W. Li, Q. Liu, D. Liu, X. Wang, J. Wang, C. Shang, R.D.K. Misra, Experimental and theoretical study on static recrystallization of a low-density ferritic steel containing 4 mass% aluminum, Mater. Des. 180 (2019) 107924, https://doi.org/10.1016/j.matdes.2019.107924.
[38] M.F. McGuire, Precipitation-hardening stainless steels, in: Stainl. Steels Des. Eng., ASM International, 2008, pp. 137–146, https://doi.org/10.31399/asm.tb.ssde.t52310137.
[39] C.-W. Chang, P.-H. Chen, K.-S. Hwang, Enhanced mechanical properties of injection molded 17-4PH stainless steel through reduction of silica particles by graphite additions, Mater. Trans. 51 (2010) 2243–2250, https://doi.org/10.2320/matertrans.M2010209.
[40] D.V. Edmonds, K. He, F.C. Rizzo, B.C. De Cooman, D.K. Matlock, J.G. Speer, Quenching and partitioning martensite—A novel steel heat treatment, Proc. Int. Conf. Martensitic Transform. 438–440 (2006) 25–34, https://doi.org/10.1016/j.msea.2006.02.133.
[41] J.-Y. Park, Y.-S. Park, The effects of heat-treatment parameters on corrosion resistance and phase transformations of 14Cr–3Mo martensitic stainless steel, in: Proc. 12th Int. Conf. Rapidly Quenched Metastable Mater., 2007, pp. 1131–1134, https://doi.org/10.1016/j.msea.2006.03.134.
[42] M. Harwarth, A. Brauer, Q. Huang, M. Pourabdoli, J. Mola, Influence of carbon on the microstructure evolution and hardness of Fe–13Cr–xC (x = 0–0.7 wt.%) stainless steel, Materials 14 (2021) 5063, https://doi.org/10.3390/ma14175063.
[43] D. Huber, L. Vogel, A. Fischer, The effects of sintering temperature and hold time on densification, mechanical properties and microstructural characteristics of binder jet 3D printed 17-4 PH stainless steel, Addit. Manuf. 46 (2021) 102114, https://doi.org/10.1016/j.addma.2021.102114.
[44] L. Emanuelli, G. Segata, M. Perina, M. Regolini, V. Nicchiotti, A. Molinari, Study of microstructure and mechanical properties of 17-4 PH stainless steel produced via Binder Jetting, Powder Metall. (2023) 1–10, https://doi.org/10.1080/00325899.2023.2202950.
[45] D. Huber, P. Stich, A. Fischer, Heat treatment of 17-4 PH stainless steel produced by binder jet additive manufacturing (BJAM) from N2-atomized powder, Prog. Addit. Manuf. 7 (2022) 187–199, https://doi.org/10.1007/s40964-021-00224-z.
[46] Y. Wu, D. Blaine, C. Schlaefer, B. Marx, R.M. German, Sintering densification and microstructural evolution of injection molding grade 17-4 PH stainless steel powder, Metall. Mater. Trans. A 33 (2002) 2185–2194, https://doi.org/10.1007/s11661-002-0050-4.